UNIVERSITAT POLITÈCNICA DE CATALUNYA
BARCELONATECH
Escola d'Enginyeria de Barcelona Est

MASTER'S FINAL THESIS

Master's Degree in Chemical Engineering – Smart Chemical Factories

PRODUCTION OF HYDROGEN BY ETHANOL PHOTOREFORMING ON TIO_2 - BASED MULTIMETALLIC CATALYSTS

Report and Annexes

Author: Daniel González Picallo

Director: Lluís Soler Turu

Co-Directora: Isabel Serrano

June 2022

UNIVERSITAT POLITÈCNICA DE CATALUNYA
BARCELONATECH
Escola d'Enginyeria de Barcelona Est

UNIVERSITAT POLITÈCNICA DE CATALUNYA
BARCELONATECH
Escola d'Enginyeria de Barcelona Est

Summary

The aim of this master's final thesis is the production of hydrogen (H_2) from a mixture containing water (H_2O) and ethanol (EtOH) by means of a photocatalytic process using TiO_2 loaded with three different metals acting as co-catalysts. This reaction was carried out in gas phase and continuous mode inside a tubular glass photoreactor containing the photocatalyst impregnated in a filter paper sheet and a light source acting as a solar simulator. H_2 generation was monitored by gas chromatography analysis with argon (Ar) acting as inert gas carrier. Several experiments were carried out, comparing different metals at different concentrations in order to study synergies between them, and also switching between UV and visible light to and assess the occurrence of the Localized Surface Plasmon Resonance (LSPR).

The work developed at the laboratory includes the design and implementation of the experimental set-up, the preparation of the TiO_2-based photocatalytic powder by ball milling technique, and the impregnation of the powder into the filter paper, as well as the performance of photocatalytic experiments and the characterization of the samples.

The performance of the samples was compared depending on parameters such as the chosen combination of metals, total metal load, metal proportions, change in the synthesis parameters, etc. Finally, the best results in terms of H_2 production were obtained with a sample of TiO_2 containing 1 wt.% of PdPtAg metals in a 35:35:30 proportion. With a gas flow rate of 20 mL/min, having H_2O and EtOH in a 9:1 proportion, and irradiating at 85 mW/cm^2 (measured at 365 nm) of UV and visible light, a maximum production of 4.73 µmol H_2/min and Apparent Quantum Yield of 4.8%, were obtained.

Resumen

El objetivo de este proyecto final de master es la producción de hidrógeno (H_2) a partir de una mezcla de agua (H_2O) y etanol (EtOH) mediante un proceso fotocatalítico usando TiO_2 decorado con tres metales distintos actuando como co-catalizadores. Esta reacción se llevó a cabo en fase gas y continuo en un fotorreactor tubular de cristal con el fotocatalizador impregnado en una membrana de celulosa y una fuente de luz actuando como simulador solar. La producción de hidrógeno se monitoreó mediante análisis de cromatografía de gases con argón (Ar) como gas portador inerte. Distintos experimentos fueron llevados a cabo, comparando diferentes metales a diferentes concentraciones para el estudio de sinergias entre ellos, así como el cambio entre luz UV y visible para evaluar la ocurrencia del efecto de Resonancia Localizada de Plasmón de Superficie (RLPS).

El trabajo realizado en el laboratorio incluye el diseño e implementación del sistema de reacción experimental, la preparación del polvo fotocatalítico con base de TiO_2 mediante la técnica mecanoquímica empleando un equipo de molino de bolas, y la impregnación de dicho polvo en un papel de filtro que actúa como soporte, así como la realización de los experimentos y la caracterización de las muestras.

La eficiencia de las muestras se comparó en función de distintos parámetros como la combinación de metales elegida, la carga total de metal, las proporciones de los metales, cambios en los parámetros de síntesis, etc. Finalmente, los mejores resultados en términos de producción de H_2 se obtuvieron con una muestra de TiO_2 conteniendo 1 % en masa de Pd, Pt y Ag en una proporción 35:35:30. Con una corriente gaseosa de 20 mL/min, con H_2O y EtOH en una proporción 9:1, e irradiando luz UV y visible con una irradiancia de 85 mW/cm^2 (medida a 365 nm), se obtuvieron máxima producción de 4.73 µmol H_2/min y Rendimiento Quántico Aparente del 4.8%.

Resum

L'objectiu d'aquest projecte final de màster és la producció d'hidrogen (H_2) a partir d'una barreja d'aigua (H_2O) i etanol (EtOH) mitjançant un procés fotocatalític usant TiO_2 decorat amb tres metalls diferents actuant com a co-catalitzadors. Aquesta reacció es va dur a terme en fase gas i en continu en un fotoreactor tubular de vidre amb el fotocatalitzador impregnat en una membrana de cel·lulosa i una font de llum actuant com a simulador solar. La producció d'hidrogen es va monitoritzar mitjançant anàlisi de cromatografia de gasos amb argó (Ar) com a gas portador inert. S'han portat a terme diferents experiments, comparant els diferents metalls a diferents concentracions per a l'estudi de sinergies entre ells, així com el canvi entre llum UV i visible per avaluar la presència de l'efecte de ressonància localitzada de plasmó de superfície (RLPS).

El treball realitzat al laboratori inclou el disseny i implementació del sistema experimental, la preparació de la pols fotocatalítica amb base de TiO_2 mitjançant la tècnica mecanoquímica emprant un equip de de molí de boles, i la impregnació d'aquesta pols al paper de filtre, així com la realització dels experiments i la caracterització de les mostres.

L'eficiència de les mostres es va comparar en funció de paràmetres com la combinació de metalls escollida, la càrrega total del metall, les proporcions del metall, el canvi en els paràmetres de síntesi, etc. Finalment, els millors resultats pel que fa a la producció d'H_2 es van obtenir amb una mostra de TiO_2 que contenia 1 % en pes de Pd, Pt i Ag en una proporció de 35:35:30. Amb un cabal de gas de 20 ml/min, amb H_2O i EtOH en una proporció de 9:1, i irradiant 85 mW/cm^2 (mesurats a 365 nm) de llum UV i visible, es va obtenir una producció màxima de 4,73 µmol H_2/min i un rendiment quàntic aparent del 4,8%.

Acknowledgements

This project has been realized thanks to the support of a number of people who have been contributing direct or indirectly during the development of the work.

First of all, I would like to express my gratitude to Lluís Soler, the director of this thesis, for offering me this opportunity and for his constant help and support. I would also like to thank the co-director, Isabel Serrano, for helping me on the laboratory for the development of the experiments.

Moreover, I would like to thank all the PhD students of the NEMEN department who shared the laboratory space with me and who helped me whenever I needed. In particular, Yufen and Asier, who shared with me their experience on previous experimentation in the field of photocatalytic H_2 production, being of vital importance for the accomplishment of this work.

Finally, I would like to thank my parents, my classmates and my partner, for their help and support during my master's degree.

Index

LIST OF FIGURES

LIST OF TABLES

UNIVERSITAT POLITÈCNICA DE CATALUNYA
BARCELONATECH
Escola d'Enginyeria de Barcelona Est

Preface

1.1. Origin and motivation of the project

This project is part of the research framework of the Nanoengineering of Materials Applied to Energy (NEMEN) group, which is part of the Polytechnic University of Catalonia (UPC) at Escola d'Enginyeria de Barcelona Est (EEBE). One of its lines of research is focused on the design and characterization of suitable photocatalysts which show high enough activity for the commercially efficient photoproduction of hydrogen from water splitting under solar light irradiation, focusing on TiO_2-based photocatalysts.

The present project is then, part of this line of research, focused on the study of the enhancement of the photocatalytic activity and enabling of visible light response of the TiO_2 by the addition of small quantities of trimetallic co-catalytic mixtures. The motivation of this study was the absence of studies about this topic, restricted only to mono or bimetallic mixtures. Then, the studies performed on this work will serve as the starting point for further research performed by the NEMEN group in this area.

1.2. Previous requirements

For the realization of this project, all the experience and information gathered with previous experimental studies carried out by the NEMEN group about TiO_2-based photocatalyst, has been used as the base of the decision-making for the development of the experimental work, including reaction conditions (e.g., quantity of photocatalyst, light intensity), synthesis procedure and parameters and also the proposed metal co-catalyst and their proportions between them and respect to the TiO_2 support.

1. CHAPTER 1: INTRODUCTION

1.1. Energy Market Current Status

In the recent years, the exponential growth of the world population and economy has resulted in a monumental increase in energy demand [1]. This fact, united with a global dependence on fossil fuels (hydrocarbons) for energy supply, has caused a massive increase in the levels of CO_2 and Greenhouse Gases (GHG) in the atmosphere, reaching CO_2 emissions from energy-related sources a maximum of 36,3 billion tonnes in 2021, 92% of them coming from carbon, natural gas and oil [2].

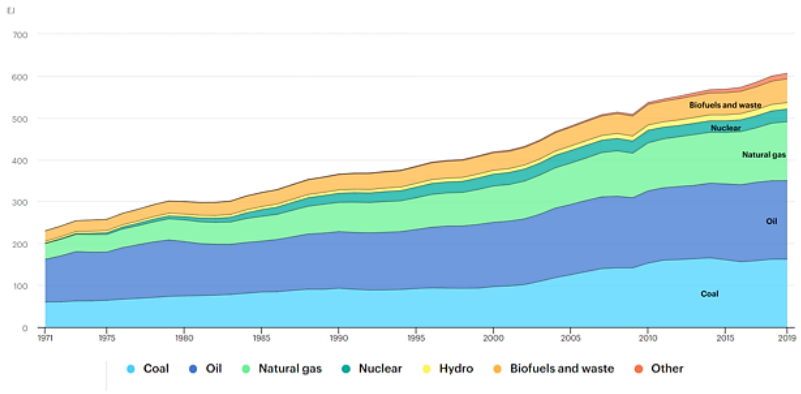

Figure 1.1. *Evolution of total energy supply by source in the last 50 years* (Source: IEA [3]).

In an effort to deal with this situation, several strategies have been developed in order to reduce these emissions, focused on the increase of the energy efficiency and the clean electrification of end-uses (such as transport and heating). However, the main challenge is still related with the decarbonisation of the energy supply by utilising alternative clean, sustainable and renewable energy [1,4].

On the other hand, transitioning towards 100% renewable energy also requires technical adaptation, as the variability and intermittency of this resources causes an imbalance between supply and demand. This imbalance also exists between the locations for consumption and production of the energy, requiring long distance and overseas transport in many cases. So, in order to maintain the stability of the electrical system, first steps are being made to implement hybrid systems comprising both renewable energy and energy storage. For this reason, it is needed to find new and environmentally friendly energy carriers that act as large-scale storage and transport systems for energy [1,5].

1.2. Hydrogen as an Energy Carrier

The concept of employing hydrogen as an energy has been the theme of research in the field for quite some time, but was strengthened following the global energy crisis of 1974 with technological advances in the 1980s [6].

Hydrogen is the most abundant and simple element of the universe, and also one of the most abundant elements in the earth's crust, always combined with other elements forming different molecules, for instance, water and most of the organic molecules. However, because hydrogen does not exist freely in nature (as lighter than air, hydrogen (H_2) molecules are not retained in the atmosphere), it can only be produced from other sources of energy, acting then as an energy carrier, a secondary source of energy that can store and deliver it as a fuel, and that can be used in transportation, in power generation systems using fuel cells, in internal combustion engines or turbines [6,7].

Moreover, hydrogen has several advantages over traditional fuels:

- The chemical energy stored in the H-H bond is easily released when it combines with oxygen, yielding only water as reaction product, making it a highly cost-efficient clean fuel, that produces zero emissions of greenhouse gases at point of use [7].
- It is the lightest element with the highest known energy content of any fuel (120 vs. 55-20 MJ/kg for conventional fuels) [6].
- It can be produced from almost all energy resources, being renewable energy sources ideal for sustainable hydrogen production [8].

1.3. Hydrogen Production

Hydrogen consumption was about 120 Mt in 2020, and is expected to rise to 530 Mt/a in 2050 [9]. Its current uses as raw chemical are mainly for petrochemical refining, ammonia production, methanol production and some power generation. However, its use as a decarbonising fuel for transportation, the buildings and heating sector and renewable energy export, is expected to raise in the following years [4]. In particular, the rise of Fuel Cell Electrical Vehicles (FCEV) technology in recent years is seen as the key step towards the introduction of the hydrogen economy, as it is often the main target in the early future studies of hydrogen [10].

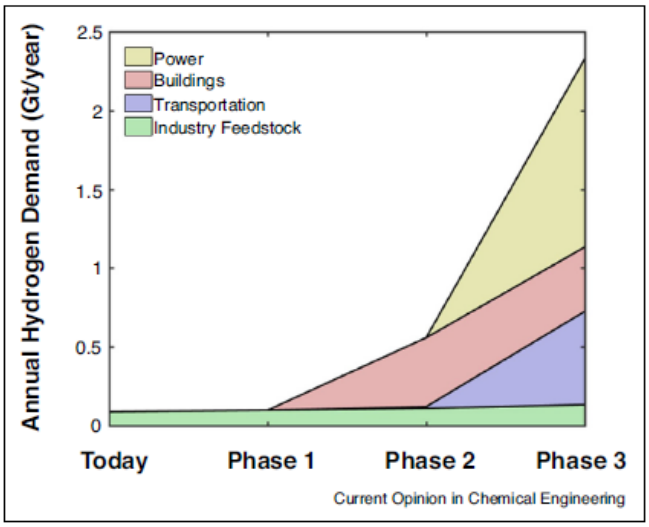

Figure 1.2. *Projections of hydrogen demand. Phase 2 based on 2030 projections, and phase 3 on predictions around 2050* (Source: A. M. Oliveira [4]).

Therefore, with the current hydrogen production happens something similar to what is happening with hydrogen consumption. As it has been mentioned before, hydrogen can be produced from a wide range of resources using different feedstock, pathways and technologies, of which many are regarded as renewable. Nowadays, though, its production is far from being sustainable/renewable, as it relies almost entirely on reforming and gasification of fossil hydrocarbon sources, such as natural gas (76%) and coal (23%), resulting in 830 Mt CO_2 annually emissions [9].So, a transition is needed in terms of the GHG emissions associated with the production process, distinguishing then different 'colours' for hydrogen:

- 'Gray' hydrogen represents the current most used technology, the one obtained from steam reforming of natural gas and/or coal (methane steam reforming, MSR). It is also referred for all the other processes which use electricity that comes from fossil fuels.
- 'Blue' hydrogen is also obtained by steam reforming of natural gas, but in this case the CO_2 is not emitted but captured and stored (CSS), usually underground.
- 'Turquoise' hydrogen is the one obtained with natural gas by methane pyrolysis, in which carbon output is as a solid.
- Finally, 'green' hydrogen is the one with zero CO_2 emissions, obtained by water electrolysis, process whereby water is split into hydrogen and oxygen through the application of electrical current generated from renewable energy sources (e.g. solar, windmills, etc.).

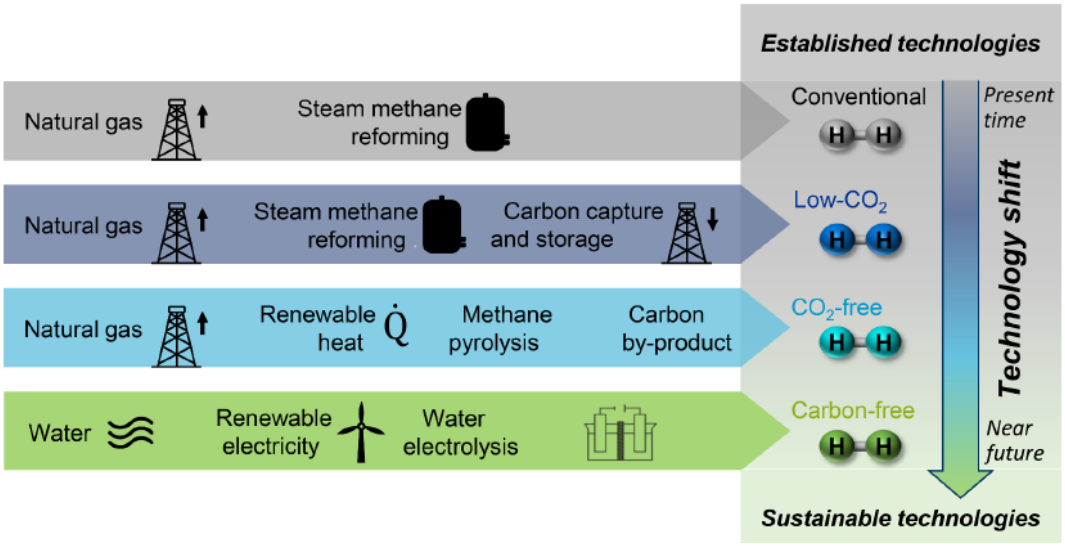

Figure 1.3. *Common colour differentiation of conventional hydrogen production pathways* (Source: M. Hermesmann [9]).

From this classification, it can be concluded that in the short to medium term hydrogen production will still rely on MSR technology, technology that will experiment upgrading with time in order to switch its colour to a more sustainable one, but in the end, it is expected that a green production by electrolysis with electricity coming from renewable energy sources will be achieved.

Water electrolysis has the advantage that produces very pure hydrogen, suitable for direct use in a Proton-Exchange Membranes (PEM) for the FCEV technology, in contrast with steam reforming, that produce a mixture of hydrogen and carbon oxides (CO and CO_2), being these membranes very sensitive to CO (threshold 10-50 ppm) and so need extra purification steps.

Apart from these colours, which represent only the most established technologies for hydrogen production at present, there are more emerging blue to green technologies base on renewable energy and resources available. For example, biomass gasification and anaerobic digestion are appealing routes that are expected to be available in the near future with a competitive hydrogen cost, being their main challenge their lower production rates. On the other hand, wind, hydroelectric, geothermal, wave and tidal energies contribution will be again based on electricity supply for water electrolysis [10].

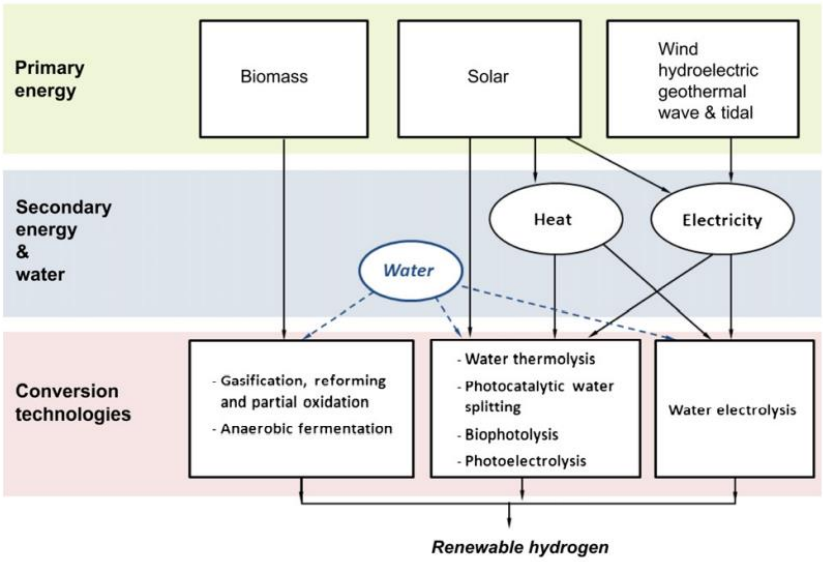

Figure 1.4. *Scheme of the main hydrogen production pathways from renewables* (Source: L. M. Gandía [10]).

Among them, solar energy is the most versatile form of renewable energy regarding hydrogen production, and contrary to typical water electrolysis, in this case the primary energy involving the water splitting is directly taken from the sun, an (almost) infinite energy source that disregard then the energy efficiency. Some related technologies are solar thermolysis, a solar-thermal water splitting consisting on direct decomposition of water driven by concentrated solar heat, biophotolysis, in which microorganisms such as microalgae that are sensible to light and exhibit hydrogen evolution capacity are cultured in a photobioreactor, or photoelectrolysis, similar to conventional electrolysis but with an electrode containing a photocatalyst that is exposed to light, allowing more compact cells and less electricity consumption [10].

In addition to those mentioned above, one solar-driven technology that is especially promising is the photocatalysis, which allows obtaining hydrogen from the irradiation of sunlight on water in the presence of a suitable catalyst that reduces the high activation energy of the decomposition reaction. The process can be carried out more easily by an indirect route, using water in combination with a so-called sacrificial reducing agent, typically, and alcohol such as methanol or even bioethanol. Noble metals such as Pd, Pt, Ag and Au supported on a semiconductor such as TiO_2 are active catalysts for this process [10]. However, the design of a tailored photocatalyst with significant efficiency to make the process commercially competitive nowadays is still a challenge, as most of the photocatalysts are only active under UV light irradiation and the activity under visible light is quite limited, having then an apparent quantum efficiency (hydrogen yield per number of incident photons) with solar light far below the 10% marked as the initial starting point for practical application. So, the low quantum efficiency is still the main ‘‘bottleneck’’ of the hydrogen production from solar light [11].

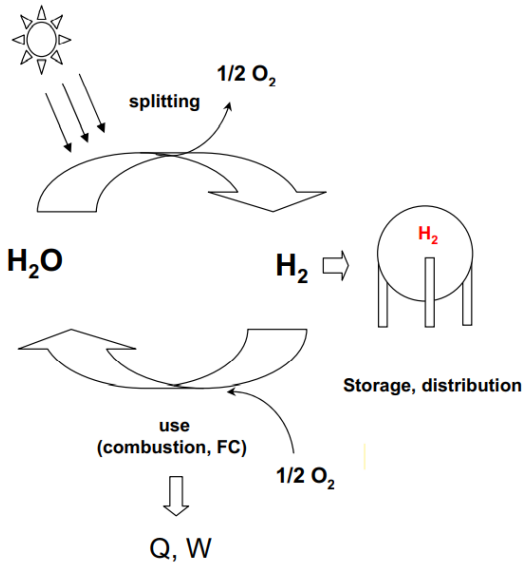

Figure 1.5. *Scheme of generation and use of solar hydrogen as energy carrier* (Source: R. M. Navarro Yerga [11]).

2. CHAPTER 2: THEORETICAL BACKGROUND

2.1. Photocatalysis

Without a consensual definition, photocatalysis is generally used to describe any process in which the rate of a chemical reaction changes due to the activation (excitation) of a substance, named the photocatalyst, by the incidence of light on it [12].Two types of photocatalysis can be distinguished:

- Homogeneous photocatalysis, when the reactants and photocatalyst are in the same phase.
- Heterogeneous photocatalysis, when the reactants and photocatalyst are in different phases.

For heterogenous photocatalysis, semiconductor materials are used as the photocatalyst, most commonly metal oxides. The principle of this process is based on the electronic structures of semiconducting materials, with an ineffective energy region with any available electronic state located between the top of the filled valence band (VB) and the bottom of the empty conduction band (CB), called band gap (BG). The photocatalyst is then activated by the absorption of a photon with the appropriate energy that is equal or higher than the band gap energy. This absorbed photon creates a charge separation with the excitation of an electron from the valence band (VB) to the conduction band (CB), creating a hole (h^+) in the VB. The electron-hole pair is called exciton, and, if not recombined, can reduce and oxidize, respectively, the electron acceptor and donor of the reactants absorbed into the surface of the semiconductor [12–14].

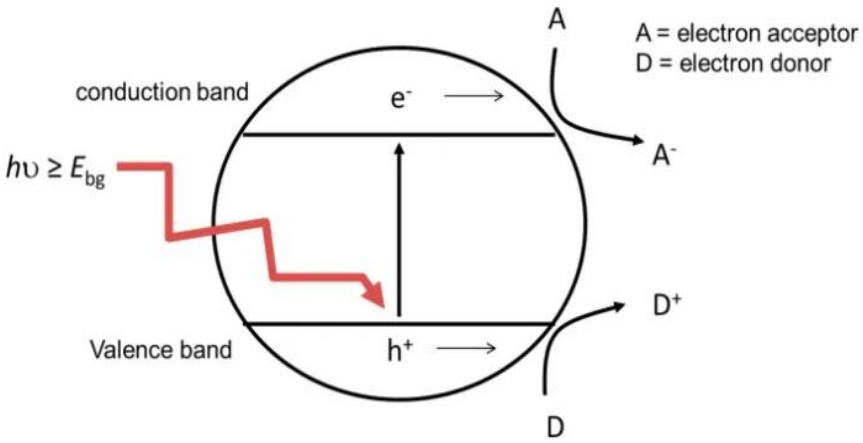

Figure 2.1. *Mechanism of a basic photocatalytic reaction* (Source: ChemistryDocs [14]).

2.2. Photocatalytic Hydrogen Production

As it has already been discussed in the previous chapter, solar light-driven water splitting to produce hydrogen has drawn increasingly attention as an efficient way to produce green hydrogen, because it does not have the inefficiencies associated with thermal transformations or with the conversion of solar energy to electricity followed by electrolysis [11].

Water splitting occurs naturally in the photosynthesis of plants, when photon energy is adsorbed and converted into chemical energy, through a complex biological pathway. To replicate this, a semiconductor acting as a photocatalyst is needed for the formation of exciton energy carriers (e^-/h^+ pair) capable of, when reaching the surface of the semiconductor without suffering recombination, reduce and oxidize the adsorbed water molecules [11]. In this redox reaction, H^+ is the electron acceptor, while water or OH^- are the electron donor species, being the overall reaction:

Oxidation $$H_2O + 2\,h_{VB}^+ \rightarrow \frac{1}{2}\,O_2 + 2\,H^+$$ (**Eq. 2.1a**)

Reduction $$2\,H^+ + 2\,e_{CB}^- \rightarrow H_2$$ (**Eq. 2.1b**)

Overall $$H_2O + h\nu \rightarrow H_2 + \frac{1}{2}\,O_2$$ (**Eq. 2.1**)

In order to achieve both water reduction and oxidation, the semiconductor must have a minimum band gap equal to the difference between the potentials of both redox reactions. Being the reduction potential of the H^+/H_2 reaction -0,41 V at pH 7 (0 V at pH=0), and the oxidation potential of H_2O/O_2 reaction 0.82 V (1.23 V at pH=0), a minimum band gap of 1.23 V is required. This energy is equivalent to the energy of a photon with a wavelength of around 1010 nm, indicating that visible light possesses energy enough for the decomposition of water [11]. However, in practice, in addition to the band structure of the semiconductor, there is an activation barrier in the charge-transfer process between photocatalyst and water molecules derived from the energy losses (transport of electron/hole, kinetic losses, electron/ hole recombination) associated with solar energy conversion, increasing the needed band gap to around 2 eV, still in the visible light range. Even so, more than only having a minimum required band gap, it also must be satisfied that the bottom of the CB must be located at a more negative potential than that of the H^+/H_2 reduction reaction, whereas the top of the VB must be positioned more positively than the H_2O/O_2 oxidation reaction [11]. **Figure 2.2** shows some examples of compliance or not of these conditions for various semiconductors:

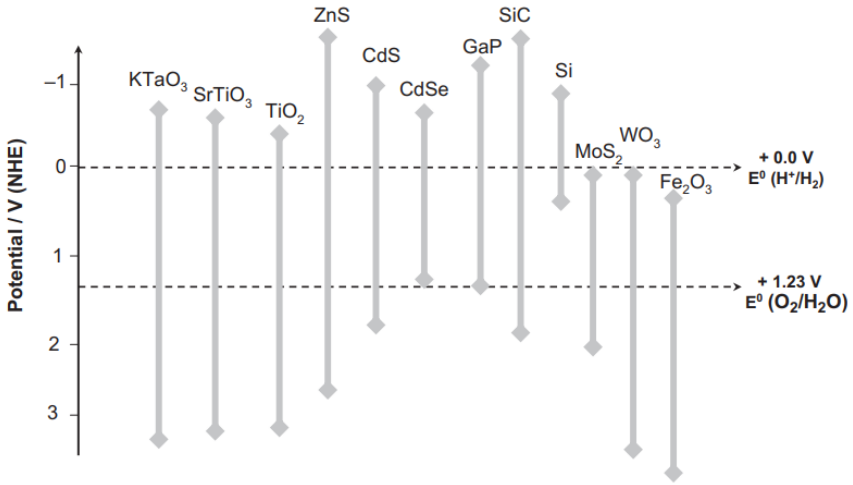

Figure 2.2. *Band gap energy and relative band position of different photocatalysts with respect to the potentials for water oxidation/ reduction reactions* (Source: R. M. Navarro Yerga [11]).

Besides having an adequate electronic structure, with a wide sufficient band gap and suitable band edge potentials, these semiconductors must satisfy other functional requirements in order to achieve an efficient water splitting:

- To have the ability to separate photo-excited electrons from reactive holes once formed.
- To minimize energy losses related to charge transport to the surface and electron-hole recombination.
- To possess chemical stability to corrosion and photo-corrosion in aqueous environments.
- To show kinetically suitable electron transfer properties from photocatalysts' surface to water.
- To have a low production cost.

Taking into account all of these requirements, titanium dioxide (TiO_2), a widely used and one of the most efficient photocatalysts, has been established as the best commercial photocatalyst for water splitting, because of its superior chemical and physical properties, such as strong oxidizing and reducing ability, high stability against photo and chemical corrosion, nontoxicity, and abundant availability in nature, which is traduced into a low cost [13].

On the other hand, in front of these advantages, TiO_2 has a high band gap of 3.2 eV (for anatase) and 3.0 eV (for rutile) that makes it optically active only under the ultra violet (UV) region of the solar spectrum, which accounts for only 4% of total solar irradiation, in front of a 49% of visible light, requiring then additional light sources for an efficient water splitting [15]. Also, it exhibits a rapid recombination of the photogenerated electron and holes, which united with a rapid reverse reaction of molecular hydrogen and oxygen to water restricts even more the reaction efficiency. To overcome this situation, several strategies have been developed in order to solve one of more of these disadvantages.

2.3. Improving Photocatalysts visible light response

As stated before, the process of water splitting is highly endothermic and requires a Gibbs free energy of 1.23 eV per electron, increased in the practice to 2 eV due to overpotentials, thus requiring a semiconductor with a higher band gap than this value, but not too high (<2.5 eV) to ensure enough absorption of radiation inside the visible range [16]. Moreover, water oxidation/reduction reactions at the photocatalyst surface may only happen if separate charge carriers (electrons and holes) generated by absorbed light can reach this surface during their life time and are capable of finding suitable reaction partners, protons for electrons and water molecules for holes. To achieve this, both generation and separation of photoexcited electrons and holes with low recombination rate is also an essential condition to be fulfilled by the photocatalyst. In order to fulfil these requirements with the TiO_2, with a too wide band gap for visible light and a high rate of e^--h^+ recombination, the applied strategies to overcome these limitations can be divided into two main approaches: band gap engineering and charge separation improvement [11].

2.3.1. Band Gap Engineering

This approach is referred to those strategies with the aim of narrowing and fine-tuning the band gap and position in order to achieve a visible light-responsive photocatalysts. Three main strategies can be distinguished in this group: cation or anion doping, heterojunction and solid solution formation.

2.3.1.1. Doping

Doping is a process of adding impurities by replacement of cations or anions in the lattice of a very pure semiconductor, providing new energy levels by the creation of new bands on the forbidden region of the semiconductor and so reducing the band gap of the photocatalyst. Depending on the replacement of cations or anions, we can distinguish between metal and nonmetal doping, respectively [17].

- Metal doping: doping of transition metal cations (Al, Cu, Cr, Fe, Ni, etc) narrows the band gap of the photocatalyst by creating an energy band (donor level) above the VB or an acceptor level below the CB of the semiconductor, facilitating absorption in the visible range. However, several studies have shown that the discrete impurities created has also a drawback, as they hinder the migration of the electron and holes acting as recombination sites [11].

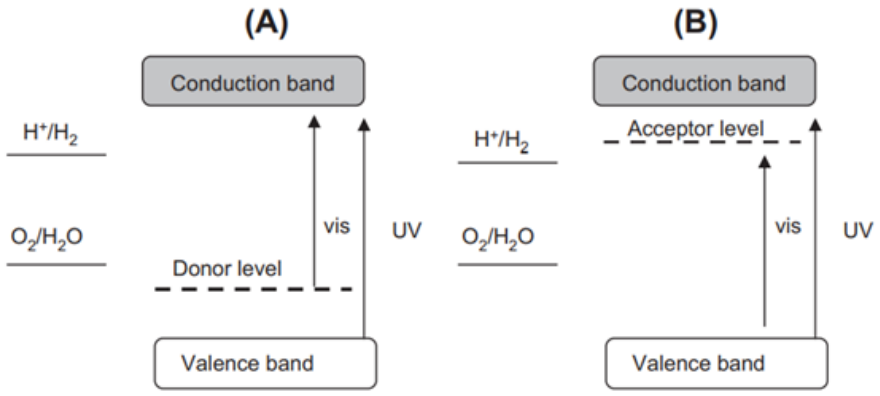

Figure 2.3. *Band structure of cation-doped photocatalyst with visible light response from a photocatalyst with UV response (donor level (A) or acceptor level (B) formed by anion doping)* (Source: R. M. Navarro Yerga [11]).

- Anion doping: in wide band gap oxide semiconductors like TiO_2, the top of the VB consists of O2p atomic orbitals. When other anions such as N, S, F or C, are introduced, they can replace these oxygen orbitals (substitutional doping) or hybridize with them (interstitial doping), which mixes the p orbitals of the doping anion with the O2p orbitals, resulting in a shift of the VB edge upward that narrows the band gap energy. Moreover, in contrast with the cation doping technique, the anionic replacement usually forms less electron-hole recombination centres, leading to a better photocatalytic activity [11].

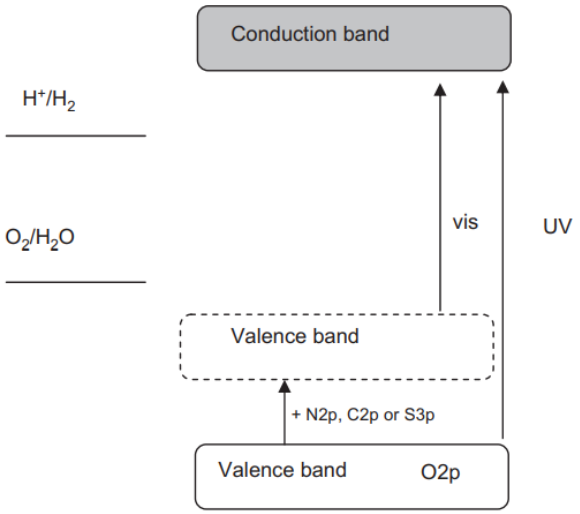

Figure 2.4. *Band structure of anion-doped photocatalyst with visible light response from a semiconductor with UV response* (Source: R. M. Navarro Yerga [11]).

- Co-doping (M-NM / M-M / NM-NM): the combination of different donor and acceptor dopants is very helpful for maintaining the charge balance, creating a synergistic effect that not only shifts the band gap to the visible region but also suppresses the recombination of photoinduced charge carriers [17].

2.3.1.2. Heterojunction

A band gap narrowing of the semiconductor photocatalysts can be achieved by combining a semiconductor of large band gap (TiO_2) with a semiconductor of narrow band gap energy and with a more negative CB level. By this, CB electrons can be injected from the visible light-responsive small band gap semiconductor to the large band semiconductor. Moreover, holes will remain in the small band gap semiconductor, suppressing the electron–hole recombination at the composite interface [11].

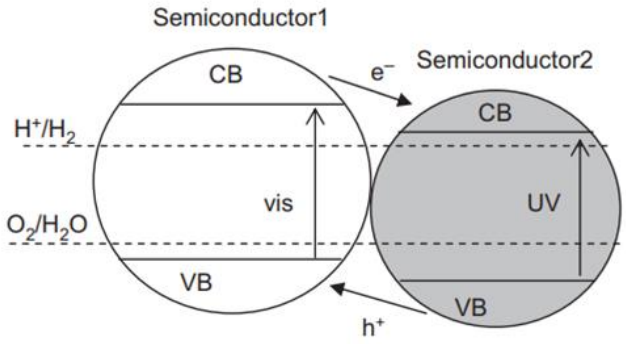

Figure 2.5. *Band structure of photocatalyst composite with enhanced visible response made from the mixture between wide and narrow band gap photocatalysts* (Source: R. M. Navarro Yerga [11]).

2.3.1.3. Solid Solution Formation

In this last approach, visible light response is achieved when two different kinds of photocatalysts with similar lattice structure are intimately mixed undergoing chemical reaction, which results in a different kind of photocatalysts with different properties than its precursors. By this technique, a visible light-responsive photocatalyst can be obtained even by the mixing of two wide band gap semiconductors [17].

2.3.2. Charge Separation Improvement

This approach is referred to those strategies apart from modifying the electronic structure and focused on the precise design of the bulk and surface properties in order to control the interrelation between its electronic, microstructural and surface properties and so achieving an efficient generation and separation of photoexcited electrons and holes with a low recombination rate.

Water-splitting reaction at the photocatalyst interface will only occur if charge carriers can reach the surface during their lifetime and manage to find and react with suitable reactants. So, first of all, the diffusion length of charge carriers must be longer than the particle size. Reducing the size of the photocatalyst then increases its performance, also due the increase in the surface area (more contact area with the reagents per mass of photocatalyst). Also, the crystal size and the crystallinity are two

important factors to tune, as the defects caused by grain boundaries act as recombination centres for the charge carriers [11]. Apart from these basic strategies, the loading of co-catalysts is a very efficient technique to promote charge separation.

2.3.2.1. Co-catalyst Loading

Deposition of noble metals (Pt, Pd, Rh, Ni, Au, Ag, Cu, etc.) or other metal oxides (e.g., NiO, RuO_2) onto photocatalyst surfaces is an effective way of enhancing photocatalyst activity. The co-catalyst improves the efficiency of photocatalysts by two manners [11]:

- By capturing the CB electron or the VB holes from the semiconductor, thereby reducing the possibility of electron-hole recombination.
- Acting as reaction sites for the reduction or oxidation of water (depending if electrons or holes have been captured) and reducing their activation energy, as having higher reduction or oxidation power then the CB or the VB of the semiconductor, respectively.

In the case of metal oxides, co-catalyst mechanism is similar than the case of coupling of semiconductors: the position of the band gaps favours the separation of the charge carriers and a co-catalyst of small band gap enables the visible light response. For noble metals, there are two main mechanisms responsible for the higher photocatalytic activity: the Schottky barrier formation and the surface plasmon resonance (SPR) [12].

2.3.2.1.1 Schottky Barrier Formation

The Schottky junction results from the contact of the noble metal and the semiconductor. This junction, called heterojunction, creates an internal electric field close to the interface metal/semiconductor, which forces the photogenerated electron and holes to move in different directions. The ohmic contact between both materials causes the electron to move from the CB of the semiconductor to the metal, supressing the electron-hole recombination, and so facilitating the transfer of holes to the semiconductor surface [12].

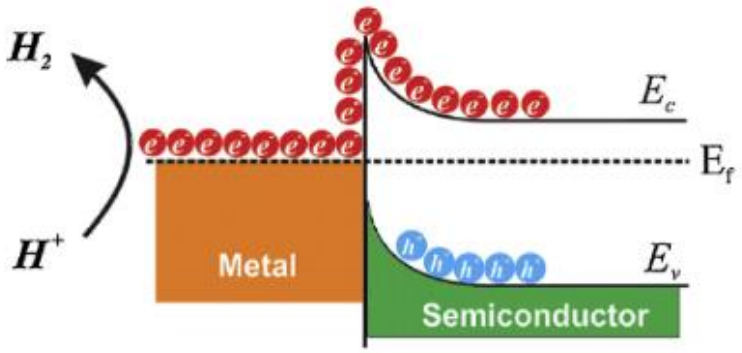

Figure 2.6. *Schematic representation of electron transfer Schottky barrier formation, where Ef indicates the position of the Fermi level* (Source: V. Kumaravel [18]).

2.3.2.1.2 Surface Plasmon Resonance (SPR)

Surface plasmon resonance occurs also when a heterojunction between noble metal nanoparticles and the semiconductor is formed, and in that case gives photocatalysts based on UV-responsive semiconductors such as TiO_2 strong photoreactivity under visible light radiation. Surface plasmons are the oscillations of the free metal electrons that can propagate at the interface of the metal and the semiconductor, induced by the radiation when the photon frequency matches the natural frequency of these electrons. When this incident light has also a wavelength higher than the size of the metal nanoparticle, an excitation of the NPs called Localized Surface Plasmon Resonance (LSPR) occurs, by which an extremely intense and highly localized electromagnetic fields is formed. The frequency of this effect can be modified by the size, morphology, proximity and nature of the metal nanoparticles [15,19].

After the excitation, the plasmons can decay non-radiatively by transferring the energy y to the electrons in the CB of the material. Highly energetic electrons (1–4 eV for the Ag or Au NPs) are thus produced, known as “hot electrons”, which can surpass the Schottky barrier and be injected in the semiconductor, leaving holes in the metal that will perform the oxidation reaction [15].

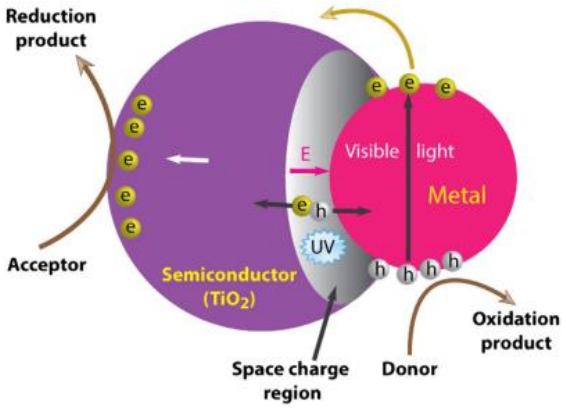

Figure 2.7. *A schematic of interface between a semiconductor and a plasmonic metal NP, charge separation, and photocatalytic activity* (Source: K. K. Paul[15]).

2.3.3. Sacrificial Agents

In an ideal photocatalytic system, the oxidation half-reaction should match well with the reduction half-reaction. However, in the case of hydrogen production, due to the proximity between the reduction potential of the H^+/H_2 reaction and the potential of the CB, this reaction proceeds at a considerably low rate and greatly limits the total photocatalytic oxidation–reduction cycle [20].

For this reason, sacrificial reductants, such as methanol and ethanol, are usually used to speed up hole consumption and slow down electron–hole recombination, although this brings several disadvantages [20]:

- Water-splitting reaction turns into a redox reaction between water and the sacrificial reductants, greatly increasing the system cost.
- Sacrificial alcohols are subsequently oxidized via a chain reaction producing CO_2, losing the process its intrinsic clean, non-carbon feature.

Nevertheless, these processes can be considered carbon neutral when bioalcohols are used as sacrificial agents, because the CO_2 emissions are counterbalanced by the CO_2 absorption by the plants that will be used to produce those sacrificial bioalcohols, closing the cycle. Therefore, bioalcohols can be understood as organic liquid hydrogen carriers.

Having said that, despite the main goal is to develop new catalysts that make sacrificial substances become unnecessary, several efforts have been made also to control the kinetics and change the pathway of ethanol oxidization into green valuable substances [20].

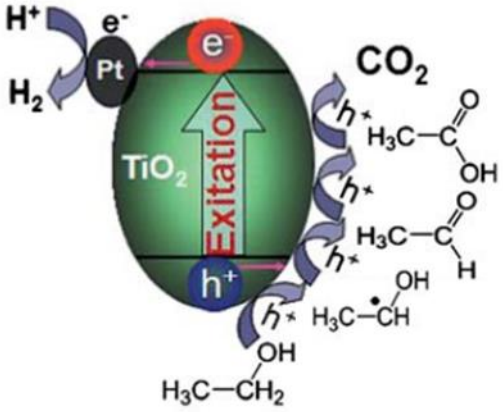

Figure 2.8. *Schematic illustration of the possible oxidation pathways of sacrificial ethanol during water splitting* (Source: H. Lu [20]).

2.4. Photocatalytic Production of H_2 from gaseous EtOH + H_2O Mixtures over Trimetallic-loading TiO_2 NPs

Once the mechanisms of H_2 production by photocatalytic water splitting, and the ways to enhance the photocatalyst performance, have been explained, this section focuses on describing the chosen reaction and conditions for the development of this experimental project.

The chosen reaction pathway for H_2 photocatalytic production has been then, by means of a gaseous reaction mixture of water and ethanol over a TiO_2-based photocatalyst, being ethanol used as a sacrificial electron donor, turning conventional water splitting into an ethanol photoreforming process. As said in previous sections, ethanol oxidation comprehends a multi-step reaction, that mainly produce acetaldehyde and hydrogen, the first one which partly further decomposes into

hydrocarbons, CO and other oxidation by-products by further photo-induced decomposition reactions [21]. The theoretical ethanol dehydrogenation (the main observed reaction) and its mechanistic steps are described below [22]:

Overall reaction $$CH_3CH_2OH \rightarrow CH_3CHO + H_2$$ (**Eq. 2.2**)

Steps:

1. Ethoxide formation $$CH_3CH_2OH + Ti^{+4}_{surf} - O^{2-}_{surf} \rightarrow CH_3CH_2O - Ti^{+4}_{surf} + OH_{ads}$$ (**Eq. 2.2a**)

2. Electron excitation $$TiO_2 + UV \rightarrow e^- + h^+$$ (**Eq. 2.2b**)

3. 1st electron injection $$CH_3CH_2O - Ti^{+4}_{surf} + h^+ \rightarrow CH_3CH^{\bullet}OTi^{+4}_{surf} + OH_{ads}$$ (**Eq. 2.2c**)

4. 2nd electron injection $$CH_3CH^{\bullet}OTi^{+4}_{surf} + h^+ \rightarrow CH_3CHO\ (g) + Ti^{+4}_{surf}$$ (**Eq. 2.2d**)

5. Hydrogen reduction $$2\ OH_{ads} + 2\ e^- \rightarrow 2\ O^{2-}_{surf} + H_2$$ (**Eq. 2.2e**)

In front of typically performed photocatalytic liquid phase reactions in water, a gas phase has been chosen to this work as a less explored area of photocatalysis but with several advantages over liquid phase, such as a higher facility to perform continuous operations, the higher separation between the process stream and the solid photocatalytic phase, that allows an easy recovery of the second one, and the more direct interaction of the light with the photocatalyst, avoiding its refraction when going through a liquid medium, especially if bubbles are formed [23].

As said before, a TiO_2-based photocatalyst has been chosen for the performance of the reaction, concretely commercial P90. As stated in previous sections, the photocatalytic activity is strongly dependant on the structure, surface and morphology of the metal oxide nanocrystals. Moreover, TiO_2 is a polymorphic material that can show mainly three different crystalline phases: anatase, rutile and brookite. Among them, rutile (3 eV) is considered to be the more stable one, while anatase (3.2 eV) is considered to be the one with superior photocatalytic activity, with lower charge carrier recombination (caused by an indirect band gap in front of the direct one of rutile). Knowing this, commercial P90 TiO_2 is formulated combining both anatase and rutile in a ca. 80:20 ratio. This particular mixture has demonstrated a higher photocatalytic activity than both pure crystalline phases independently employed. The reasons owing to this higher photocatalytic activity are not only because of the tuning of their structure and morphology, but also because of a better charge carrier separation when both crystalline phases are simultaneously employed, enhancing the lifetime of charge carriers, which improves the reaction yield [24,25].

Also, in order to enhance even more the photocatalytic activity and achieve visible light response, different strategies have been implemented to modify the interaction between the metal (acting as a cocatalyst) and the semiconductor (acting as a support). Most works focus on the assessment and comparison of the improvement on this activity by the addition, one at a time, of different metals acting as cocatalysts, normally noble metals such as Pd, Pt, Rh, etc., or whether the visible response is achieved or not, normally with Au, Ag or Cu, among others. Some of the prior works reported experiments with simultaneous loading of two of these metals [26–29], but at the best of our knowledge no reports are available with three or more at the same time to perform a photocatalytic hydrogen production at the gas phase under continuous operation.

2.5. Objectives and Scope of the Project

Taking into account what has been mentioned before, the intention of this work is then the production of H_2 using a water-ethanol mixture by means of a heterogeneous solid-gas photocatalytic process in a tubular reactor, using a TiO_2-based photocatalyst simultaneously loaded with three different metals as co-catalysts, in order to study synergetic effects between them that could enhance the photocatalytic activity achieved. Two of them; Pd and Pt, are intended to extend the lifetime of the charge carriers by trapping the generated electrons by means of a Schottky barrier formation, acting as the active sites for the reduction reaction (**Figure 2.8**), while the last one, Au, Ag or Cu depending on the experiment, is expected to show a Localized Surface Plasmon Resonance (LSPR) effect and give to the photocatalyst a visible light-response capacity. The scope of this work will include:

- The design and implementation of the experimental set-up.
- The preparation of the photocatalyst samples.
- The assessment and election of the 3rd loaded metal (Au/Ag/Cu).
- The comparison of the photocatalytic performance between different samples of the 3 chosen metals, changing the proportions between them and their quantity on the support and also the synthesis parameters.
- The comparison between the obtained H_2 production under Visible and/or UV light irradiation.
- The characterization of the prepared samples by microscopic and spectroscopic techniques.

3. CHAPTER 3: EXPERIMENTAL SECTION

In this chapter, all the experimental work, including the design and build up of the process layout, the preparation of the photocatalyst and the performance procedure of the experiments, is presented.

3.1. Process Layout

For the performance of the experiments, a simple, small-scale process circuit was built from scratch. **Figure 3.1** shows the general layout of the final experimental set up. The circuit starts with an inlet of inert gas (argon, Ar) coming from the available gas lines in the laboratory. This $Ar_{(g)}$ inlet, regulated to the desired value by a mass flow controller (*1*), enters a bubbler (*2*), where the inert gas is dispersed through a liquid solution of water and ethanol, obtaining a gaseous mixture of these two compounds of a 9:1 molar ratio of water and ethanol, respectively. Once achieved the desired stream of reactants, it enters to the photoreactor (*3*), where it goes through a circular sheet of a filter paper (*4*), which has been previously impregnated with the photocatalyst and where artificial light (*5*) (UV or UV + visible, depending on the experiment) is irradiated by a solar light simulator (*6*). Finally, the resultant gaseous stream with the reaction products is send to a gas chromatography equipment (*7*), where the composition of the outlet is continuously monitored in order to evaluate the photocatalytic performance of the studied samples.

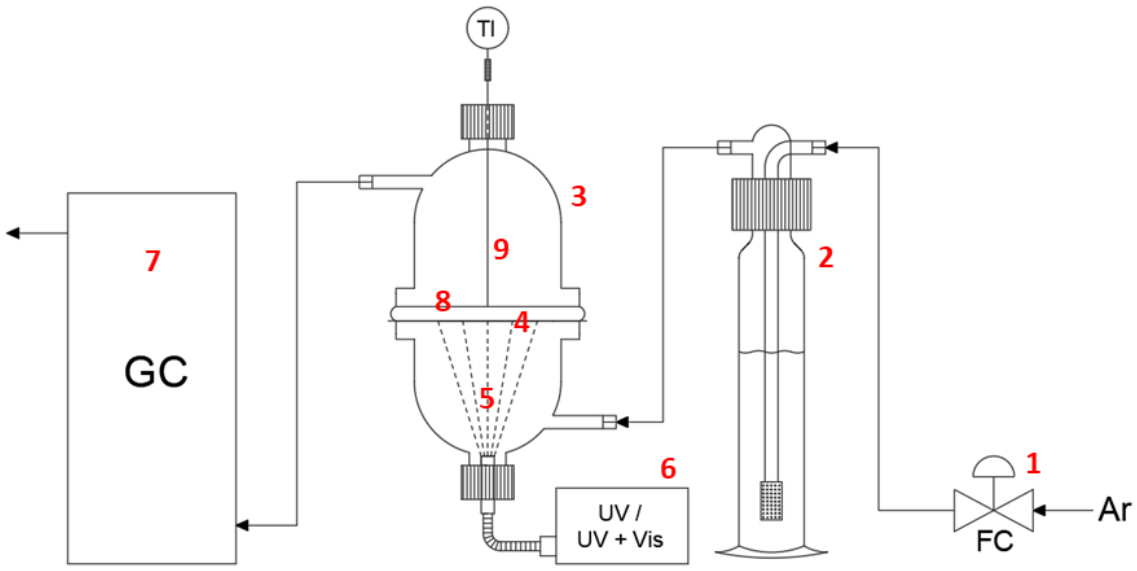

Figure 3.1. *Layout of the experimental photocatalytic reaction system.*

The resultant photocatalytic reaction system constructed from this layout can be seen in **Annex A**.

3.1.1. Mass-flow Controller

For the setting of the flow of gases at a constant rate, a mass-flow controller **MASS-STREAM™ series D-6300**, from **M+W INSTRUMENTS GmbH**, has been used. The setpoints of the mass flow controller were initially calibrated with different $Ar_{(g)}$ flow values, in order to determine a calibration curve of the mass flow controller.

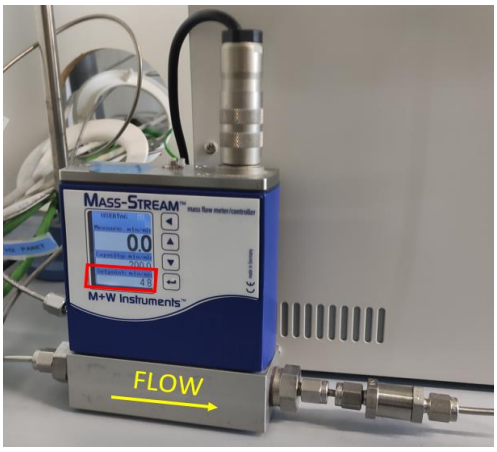

Figure 3.2. *MASS-STREAM™ series D-6300, already mounted and with the desired set-point (red).*

3.1.2. Glass Bubbler

A dreschel bottle from AFORA^{TM} has been used as a bubbler. In order to achieve the 20 mL/min flow with a 9:1 water-ethanol molar ratio in the gas phase, a mixture liquid of these two compounds with 18.14 g of ethanol and 160 g of water has been introduced into the flask, following Raoult's law and Riedel equation. The ground glass connection, that allows the sealing of the equipment, has been filled with silicon grease in order to allow the opening of the equipment for the mixing refilling once a month.

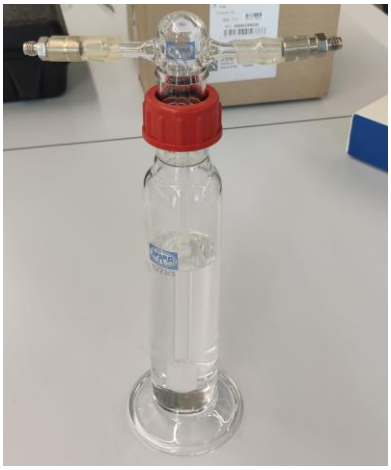

Figure 3.3. *Bubbler prepared with the EtOH:H_2O solution and its gastight Swagelok® connections.*

3.1.3. Photocatalytic Gas-phase Reactor

For the construction of the gas phase reactor, two cylindrical reaction flasks from VIDRAFOC, each of them having a flow entry/exit on the sides and one opening closed by a screw cap, have been coupled, placing the filter paper photocatalyst between them. Also, to avoid nearly direct glass to glass contact and to seal the equipment in order to avoid leaks, an o-ring, made of Polydimethylsiloxane (PDMS) has been synthesized and placed afterwards between both glass photoreactor flasks (***Figure 3.1**, nº 8*). Finally, in order to keep all the pieces together and again seal the equipment, these flasks have been wrapped in Parafilm® and then pressed against each other (with the O-ring between) with two 3D printed plastic pieces joined by screws, acting as a clamp.

***Figure 3.4.** Reactor halves, PDMS O-ring and some of the used 3D printed pieces.*

The inlet of gas has been connected to the side entry of the bottom flask, while this same entry in the upper flask has been used as the outlet of gas. In the case of opening closed by screw caps, these caps have been pierced in order to insert two devices in the equipment: a thermocouple in the upper part and the light guide of the light source in the bottom part. Photos of the final assembly of the reactor can be seen in **Annex A**.

3.1.3.1. Polydimethylsiloxane (PDMS) o-ring

For the fabrication of the PDMS o-ring, the commercial silicone elastomer kit, **SYLGARD™ 184**, from **DOW CORNING**, has been employed. This kit consists of two different chemicals: the elastomer (Part A) and the curing agent (Part B). As said in the product specifications, they should be mixed in a A:B 10:1 weight ratio. So, the followed steps for its fabrication have been the following ones.

1. Knowing required quantities from previous experiences, 5 g of the elastomer, and after it 0,5 g of the curing agent, have been weighted in the same beaker and stirred during 5-10 min until we achieve a uniform mixture.
2. Then, the mixture has been placed inside the vacuum chamber during 10-20 min, degassing the dissolved air in the PDMS mixture during the stirring.

3. Once we do not observe more evolution of bubbles, the mixture has been poured into a 3D printed circular mold, specifically printed with the desired o-ring measures for this type of reactor. The pouring has been done slowly and gently, checking that no bubbles appear inside the mixture in the mold, as they may act as initiating points of cracking when the O-ring will be subjected to stresses.
4. Finally, the mixture was left to cure in the mold for 48 h at ambient temperature, or in case of an urgent need of the O-ring, it can also be cured in a furnace at 100ºC during 35-45 minutes [30].

3.1.3.2. Light Source

In order to irradiate visible and/or UV light into the photocatalyst sample at a controlled and known intensity, an artificial light source has been used, concretely the **L9588 LightningCure** spot light source model **LC8**, from **HAMAMATSU**. This equipment, with high intensity mercury-xenon lamps, is a solar simulator lamp that can emit light in the UV + Visible spectrum (indeed simulating the solar light spectrum). Additionally, by the placement of a light filter inside the equipment, the resultant spectrum can be selected to only emit UV radiation, making possible the comparison of the photocatalytic activity with UV or visible light in order to determine if SPR occurred in the performed experiments [31]. The hosting group had no previous experience with this light, so the assembly of all the components (light guide, lamp, etc.), the tuning of the parameters and the coupling of this light to the photocatalytic reactor has been done for the first time.

Figure 3.5. *Light source LC8 from HAMAMATSU.*

Moreover, this equipment has an operation panel where the intensity of the light can be manually modified in order to choose the desired irradiance (this can be done also remotely from a computer, and even an irradiation program can be set). In order to know the value of irradiance reaching the photocatalyst depending of the % of intensity of the equipment, calibration tests with and without

the UV filter have been performed, being the results shown in **Figure 3.6**. To do so, the different UV irradiances were measured by an UVA radiation monitor (Solar Light Co.).

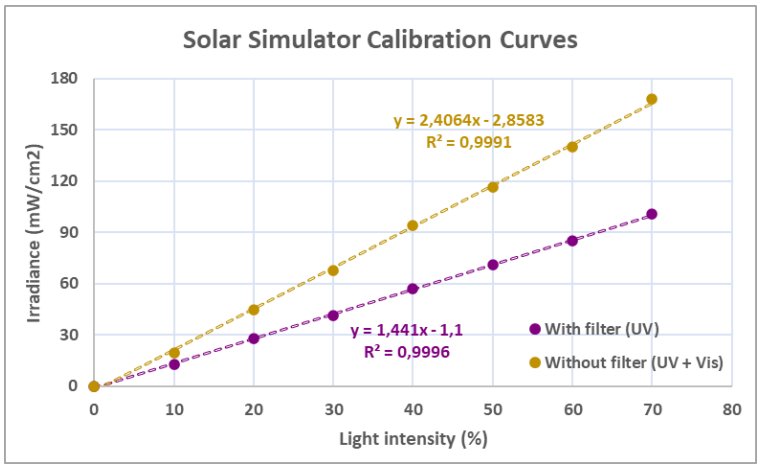

Figure 3.6. *Calibration tests of irradiance for the LC8 solar simulator.*

3.1.3.3. Thermocouple

An **RS PRO type k** thermocouple has been used to measure the temperature at which the reaction takes place. To do so, it has been introduced in the reactor (***Figure 3.1****, nº 9*) in a way that the tip of the thermocouple just touches the filter paper, without passing through it. To fix this position, Parafilm® and superglue has been used, also to seal the created hole in the upper plastic cap used as a reactor feedthrough. In order to register and store the temperature measurements during the experiments, the thermocouple has been connected to the **USB TC-08** 8-channel thermocouple data logger, from **PICO Technology**, whose software allows the obtention of the evolution of temperature over time in graphs and tables.

3.1.4. Gas Chromatography

The analysis of the H_2 and other compounds produced in the reaction is carried out by the gas chromatograph model 490 Micro GC, from AGILENT TECHNOLOGIES. It is a rugged, compact analyser for gas quality on-line (and also at-line) analysis in the laboratory, and can be easily controlled through a PC. The micro-machined injector and thermal conductivity detector (μ-TCD) together with a narrow-bore column, deliver separations of gases in a matter of seconds, allowing the obtention of rapid results while performing the experiments [32].

As it is well-known, gas chromatography is a simple and effective widely used for quantitative and qualitative analysis of mixtures, based on the difference of the degree of interactions between each constituent of the sample, the flowing mobile phase, and the stationary non-volatile phase that the sample passes through: the greater the interactions, the more time will spend the constituent until getting eluted from the stationary phase. This, united with the TCD, which senses the changes in the

thermal conductivity of the column effluent and compares it to a reference flow of carrier gas (the argon), detects the times at which the analytes elute from the column and produce a voltage signal proportional to their concentrations. Finally, these signals are transformed into time-displayed peaks in a chromatogram, that when integrated give the relative concentration (%) of the analyte, recognized by its characteristic elution time in a certain type of column [33,34].

For the detection and analysis of the reaction products of these experiments, the 490 Micro GC is equipped with 3 channels with 3 different columns, each one of them operating independently for the analysis of different groups of compounds [32]:

- **Channel 1**: Molsieve 5Å 10 m Heated column (**10 m MS5Å**), designed to separate: H_2, CO, CH_4, N_2, O_2, and some noble gases.
- **Channel 2**: PoraPlot u 10 m Heated column (**10 m PPU**), designed to separate hydrocarbons C1-C6.
- **Channel 3**: CP-WAX 52 CB 4m Heated column (**4 m 52CB**), designed for low boiling point analytes (i.e., alcohols).

The reaction products were monitored by the GC every 4 minutes of operation during all the photocatalytic experiments performed.

3.1.5. Connections

In order to carry the gas flow through the entire circuit and thus connect the process units to each other, the needed pipelines had also to be built. To do so, AISI 316L Swagelok tubes of 1/8'' diameter and their gastight ferule fittings have been used. The raw pipes have been cut to the desired size and bent to the desired shape, and female fittings have been inserted at their ends, while male fittings have been placed in the inlets and outlets of the different units (reactor and bubbler), adjusting them with plastic tubes. By this montage, an easily detachable and pluggable circuit, for the replacement or cleaning of the units, has been obtained.

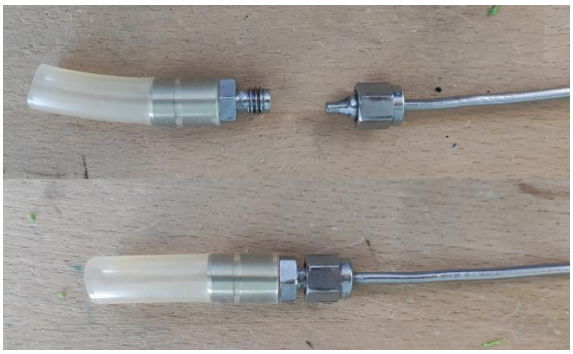

Figure 3.7. *Fabricated tubing and connections (upper components: detached Swagelok® connection; and lower components: plugged gastight Swagelok® connection).*

3.2. Photocatalyst Synthesis

As mentioned in the previous chapters, the photocatalyst employed for the performed experiments is a P90 titanium dioxide (TiO_2)-based catalyst with 3 different metals loaded on it acting as co-catalysts: Platinum (Pt), Palladium (Pd) and a third one varying between Gold (Au), Silver (Ag) and Copper (Cu), depending on the experiment. For its synthesis, a simple method, ball milling, has been used.

Ball milling is a well-known solventless method for decreasing the size of particles that presents several advantages such as simplicity, versatility and scalability. In addition to decreasing the particle size, ball milling can be also employed to perform chemical transformations induced by mechanical forces by the so-called mechanochemistry, which enables the use of insoluble reagents. In comparison to that, the typical manufacture of heterogeneous catalysts integrating one or more co-catalysts over oxide supports typically involves several steps in liquid phase that could compromise the scalability and control of their industrial production [35].

So, for all these reasons, mechanochemistry is probably the simplest, fastest and environmentally-friendly method for preparing catalysts, and has been recently rediscovered as a promising method to produce highly active heterogeneous catalysts, which are not available by conventional synthesis routes. Also, their use for the preparation of the desired photocatalysts for this work is consolidated by its use for similar experimental works performed by the PhD students of NEMEN research group in the same EEBE-UPC laboratory [35].

3.2.1. Synthesis Reagents

Commercial AEROXIDE® TiO_2 P90 (80% anatase and 20% rutile, purity > 99.55%), produced by EVONIK INDUSTRIES, has been employed as main photocatalyst. As salt precursors for the metal co-catalysts, the following compounds have been used:

- Palladium(II) acetate [$C_4H_6O_4Pd$], 47.5% Pd, from ACROS ORGANICS (now THERMO SCIENTIFIC™)
- Platinum(II) acetylacetonate [$(C_5H_7O_2)_2Pt$], 98%, from ACROS ORGANICS / THERMO SCIENTIFIC™
- Gold(III) acetate [$C_6H_9AuO_6$], 99.9%, from ACROS ORGANICS / THERMO SCIENTIFIC™
- Silver nitrate [$AgNO_3$], ≥99%, from SIGMA-ALDRICH
- Copper(II) nitrate 3-hydrated [$Cu(NO_3)_2 \cdot 3\ H_2O$], from SIGMA-ALDRICH

Also, for the impregnation of the powder into the filter paper, absolute ethanol (EtOH) from SCHARLAU, has been used.

3.2.2. Ball-milling Equipment

For the milling of the samples, the Mini-Mill Pulverisette 23, from FRITSCH, has been used. This equipment ensures high performance on the comminution of small quantities of a wide range of samples using a spherical grinding bowl with one or more grinding balls. Inside it, samples are grinded through the impact and friction between grinding balls and the inside wall of the grinding bowl, achieved by vertical 9 mm amplitude oscillations. The frequency of these oscillations can be fixed between 900 and 3000 times per minute, as well as the oscillation time, between 1 and 60 minutes [36].

For the preparation of our samples, a 10 mL grinding bowl made of stainless steel, and a unique 15 mm grinding ball of the same material, have been used.

Figure 3.8. *Ball mill equipment and used grinding ball and bowl.*

3.2.3. Synthesis Procedure

First of all, the required amounts of each reagent have had to be determined. From previous experiences with similar experiments, a ball to powder ratio of 45 [35,37] have been set as the quantity of metals + TiO_2 / total powder to be introduced in the grinding bowl. This value has been determined through previous experiences as the balance point between having too much powder, which would lead to restricted movement of the grinding ball within the bowl, and too little powder, which would result in insufficient collision force between the particles [35,37].

Knowing the weight of the ball:

$$Metals + TiO_2\ powder = \frac{16{,}5558\ g}{45} = 0{,}3679\ g \qquad \textbf{(Eq. 3.1)}$$

For the calculation of the quantity of each reagent, the co-catalysts loading had to be set first. Loadings of 1, 1.5 and 2 wt.% has been used in this work, with metals proportions of 35% for both Pd and Pt, and 30% for the third metal. Previous works with Au/TiO_2 reported best reaction rate per loading % at 1 wt.% [22], but the 1.5 wt.% has been established as the starting point of these experiments, as due to the division of the loading between different metals, low % loadings lead to very low quantities of required salt weights that the available scale cannot measure without a considerable error (measure threshold 0.1 mg, <0.2 mg the errors can be very important). Knowing molecular weights of both salts and pure metals, and the purity of these salts (***Table 3-1***), the required quantity of salt to achieve the desired loading of each metal has been calculated by means of the following equation:

$$Salt = Total\ powder \cdot \%\ loading \cdot \frac{\%\ metal}{100\%\ metals\ loaded} \cdot \frac{MW\ salt}{MW\ metal} \cdot \frac{1\ mol\ salt}{n\ mol\ metal} \cdot \frac{100\%\ salt\ powder}{\%\ pure\ salt} \qquad \textbf{(Eq. 3.2)}$$

Also, for the required TiO_2 for each loading:

$$TiO_2\ powder = Total\ powder \cdot (1 - \%\ loading) \qquad \textbf{(Eq. 3.3)}$$

Table 3-1. *Molecular weight and purity of metals and their salts.*

Metal salts	MW metal (g/mol)	MW salt (g/mol)	Purity salt
$(C_5H_7O_2)_2Pt$	195,08	393,30	98%
$C_4H_6O_4Pd$	106,42	224,51	99,9%
$C_6H_9AuO_6$	196,97	374,10	99,9%
$AgNO_3$	107,87	169,88	99%
$Cu(NO_3)_2{\cdot}3H_2O$	63,55	187,55	99,9%

The obtained values for each loading % can be seen in the following table:

Table 3-2. *Required quantities of TiO_2 and metal salt powder for each % of loading.*

	% loading	1%	1,5%	2%
	TiO_2	0,3642 g	0,3624 g	0,3605 g
1st metal	Pt salt	0,0026 g	0,0040 g	0,0053 g
2nd metal	Pd salt	0,0027 g	0,0040 g	0,0054 g
3rd metal	Au salt	0,0021 g	0,0031 g	0,0042 g
	Ag salt	0,0018 g	0,0026 g	0,0035 g
	Cu salt	0,0033 g	0,0049 g	0,0065 g

Once the quantities were determined, the procedure explained below has been followed for the preparation of the photocatalyst:

1. Firstly, all these required quantities have been measured on a 0,1 mg-threshold scale, over a filter paper.
2. When measured, all the reagents have been carefully deposited inside the grinding bowl. After that, the grinding ball has also been introduced into the vessel, being careful to not spill the powder.
3. Then, the grinding bowl has been closed and placed on the ball milling machine. Here, the two ball milling parameters, milling time and milling frequency, have had to be fixed. The milling time could promote the mechanochemical reaction and influence the dispersion or particle size of the catalyst, modifying its specific surface area and the number and quality of active sites. However, when the milling time exceeds a certain range, the agglomeration of particles may be induced and many surface defects can be generated, which could accelerate the recombination rate of electron-hole pairs, reducing the photocatalytic performance. Respect to the milling frequency, it is also an important parameter due to its influence on the efficient mixing of the photocatalyst components. High-energy mechanical forces could help the incrustation of the metals and the reduction of the particle size, but could also result in the formation of structural defects, which act as effective recombination centres of electron- hole pairs. Moreover, excessive incrustation can cause the encapsulation of metals by the TiO_2 support, which would result in a decrease of the photocatalytic activity. So, again, the results have been decided following previous experiences, choosing 10 min of milling with the minimum frequency given by the equipment, 15 Hz [35,37].
4. Once finished, the vessel has been removed from the equipment and opened again. The resultant photocatalyst powder has been peeled off the vessel walls and stored in a small jar,

adequately closed and wrapped in aluminium foil in order to avoid the minimum contact with oxygen and light.

As said in before, for the performance of the experiments, this resultant powder, which is already the final photocatalyst, has been impregnated into a filter paper through which the reactant gaseous flow will pass in order to perform the photocatalytic reaction. For the preparation of these impregnated filter papers, the following steps have been carried out:

1. In the first place, filter paper circles equal to the outer diameter of the glass photoreactor have been cut, also drawing an inner circle equal to the inner diameter of the photoreactor (4 cm) with a pencil. This drawn circular contour will help the powder not to spread outside it, losing active sites.
2. In parallel, 26.1 mg of the prepared powder have been measured in the scale inside a 1.5 mL Eppendorf™ microtube. This quantity has been reported by previous experiments in the group as the optimum quantity of photocatalyst for this illuminated area, in order to achieve the maximum apparent quantum yield, which does not depend on the amount of the photocatalyst loaded but on the irradiated area.
3. Once measured, around 1 mL of ethanol has been added to the cylinder in order to suspend the powder by intense agitation with an ultrasounds equipment. Then, a 10-100 µL micropipette has been used to pour the suspension into the filter paper, taking care not to exceed the drawn contour and to do it as uniformly as possible. This process has had to be done several times until emptying the 1 mL of ethanol, letting dry the poured one inside an oven (50-60ºC) each time the liquid soaked the filter paper. Also, after emptying the initial ethanol suspension, one or two small volumes of ethanol have been added again to the cylinder and poured into the filter paper to ensure the impregnation of the entire powder. Finally, after letting the paper in the oven during 10 min approx. in order to remove all the ethanol, the final sample of impregnated photocatalyst is obtained.

Regarding illustrative description, a photographic report of the explained procedures can be seen in **Annex A**.

3.3. Other Tasks prior the Photocatalytic Experiments

Before starting the experiments, several checks have been made in order to ensure the accuracy and precision of the obtained results. These checks have been mainly focused on the avoidance of leaks in the system. Gases, especially hydrogen (due to its small size), tend to leak through fittings and connections very easily when the sealing is not good enough. This probability of leakage is accentuated due to the overpressure created upstream to the gas chromatography equipment, due to the presence of a pipe constriction on this equipment.

As said before, to ensure their avoidance, all identified points with a potential risk of leaks (plastic tubes with the male fittings at the outlets and inlets of the bubbler and the reactor, the union between the two halves of the reactor, thermocouple, light source, etc.) have been wrapped with Parafilm® conscientiously.

After that, in order to ensure that no leaks are present on the system, as the circuit has been assembled, it has been checked that the flow rate is maintained at 20 mL/min after each equipment connection, in order to locate more easily the leakage points, if any. Again, in the case of the union between the two halves of the reactor, this check has had to be done every time before starting an experiment, as all the sealing there has to be removed and remade to place the new sample of photocatalyst.

For the measurement of these 20 mL/min of flow, a manual soap bubble flow meter has been used. This simple device, consisted by a thin column with marked volumes (each millilitre) and a small rubber balloon filled with soap in their lower end, when connected to the point of the circuit where the flow is intended to be measure (i.e., after the bubbler, after the reactor and finally after the GC), can allow us to do it by squeezing the rubber, generating a bubble that will ascend through the column pushed by the gaseous stream at its same velocity. Then, by simply measuring with a chronometer the time it takes to ascend a certain volume (the larger, the smaller the error), the flow can be obtained:

$$\left(20\ \frac{mL}{min} \cdot \frac{1\ min}{60\ s}\right)^{-1} = \mathbf{3\ seconds\ per\ mL\ of\ column\ ascended} \qquad \textbf{(Eq. 3.4)}$$

So, a value above this value is obtained, it would mean the presence of leaks on the system.

Figure 3.9. *Manual soap bubble flow meter.*

3.4. Experimental procedure

Once the photocatalyst has been introduced and the reactor has been closed and sealed with the absence of gas leaks, the experiment is ready to begin. To start running it, the $Ar_{(g)}$ line´s valve has been opened, and from the computer software, the GC has been switched from the usual rest mode to the analysis one, introducing a method previously designed for the correct detection of the substances present on the product stream to be analysed. This method has been improved with the first runs of experiments, checking that all elution times are correctly set and related with the right specie.

Then, the GC analysis has been started, with a sampling frequency of 4 minutes that continuously monitored the reaction products. Before turning on the light (either UV or UV + Visible), it is needed to wait around 10-15 samplings, as the GC is saturated with air and shows very high levels of O_2 and N_2 at the beginning. This peak of O_2 is final check and also the monitor value regarding the existence and/or appearance of leaks in the system during the experiment, needed to be around or below the 0,01%. This is very important, as due to the equilibrium reaction of photocatalytic water splitting (**Eq. 3.5**), higher levels of O_2 would shift the equilibrium to the reverse reaction (formation of water, according to le Chatelier's principle), so decreasing the production levels of H_2 (which already happens with the 0,01%, but in a small amount, decreasing to 0,06-7%):

$$H_2O \rightleftharpoons H_2 + 1/2\ O_2 \qquad \textbf{(Eq. 3.5)}$$

Once lowered and stabilized the O_2 level, the light has been switched on, starting the reaction in the photocatalyst. The time at which this light is switched on will correspond to t = 0 on the graphically displayed results of this work (see **Chapter 4**), as being the samples taken until then meaningless for results comparison. GC samples have been taken during 1-2 hours for each run or light step (in case of being two or more in the run, letting some time with the lights turned off between them) in order to let the production to stabilize. After that, light has been switched off, the GC sampling has been stopped by turning it back to rest mode, the $Ar_{(g)}$ line has been closed and the reactor has been dismantled for the introduction of a new photocatalyst sample.

3.5. Evaluation Parameters

For the evaluation of the performance of the photocatalyst samples, the global efficiency of the system, the comparison between samples and also the comparison with previous works, two different parameters have been used: the H_2 production rate (overall and normalized with the photocatalyst mass) and the Apparent Quantum Yield (AQY).

3.5.1. Hydrogen Production Rate

This parameter will be the most important and used one, as being the main goal of this work. As described before, the results obtained from the gras chromatography analysis are given in relative concentration of the analyte (‰). In order to obtain the production rate of hydrogen in µmol/min, the following equation has been used:

$$r_{H_2} = G \cdot \frac{\%_{H_2}}{100} \cdot \frac{P}{R \cdot T} = G \cdot 1000 \cdot \frac{\%_{H_2}}{100} \cdot \frac{1}{24{,}4} \quad \left[{}^{\mu mol}/_{\min}\right] \qquad \textbf{(Eq. 3.6)}$$

being G the gas flow, $20\ mL/min$, $\%_{H_2}$ the relative concentration of hydrogen given by the GC, P and T the normal conditions of pressure and temperature (1 atm and 298 K) and R the gas constant ($0.082\ atm \cdot L/(mol \cdot K)$).

This hydrogen production rate can also be expressed per weight of photocatalyst, which allows to compare the photoactivity with different quantities of photocatalyst, allowing the normalization of the results in case of losses during impregnation or for the final comparison with other experimental works:

$$r''_{H_2} = \frac{r_{H_2}}{m} \quad \left[{}^{mmol}/_{\mathrm{h} \cdot \mathrm{g}}\right] \qquad \textbf{(Eq. 3.7)}$$

where m would be the quantity (in grams) of photocatalyst in the sample. The chosen units in this case were different, following the typical displayed ones in other existing reports.

3.5.2. Apparent Quantum Yield (AQY)

This parameter represents the efficiency of the photocatalytic process in photonic terms, and is defined as the ratio between the number of photons emitted by the incident light on the sample and the number of photons which are absorbed by the catalyst and successfully yield into photocatalytic products (that is, the number of generated e-/h+ pairs that are efficiently separated and participate in the redox reactions without recombine). As said before, the obtained value for this parameter is very important, as it will show how far is the assessed sample from the marked 10% value (referred to visible light) of this parameter as the initial starting point for practical application [11].

As seen in **Equations 2.1** and **2.2**, two incident photons are required to generate two excitons with two electrons in order to produce one molecule of hydrogen. Then, Apparent Quantum Yield will be calculated as:

$$AQY(\%) = \frac{n^{\underline{o}}\ reacted\ e^-}{n^{\underline{o}}\ incident\ photons\ (\gamma)} \cdot 100 = \frac{2 \cdot n^{\underline{o}}\ produced\ H_2 molecules}{N_\gamma} \cdot 100 \qquad \textbf{(Eq. 3.8)}$$

Developing each term of the equation:

$$nº\ produced\ H_2 molecules = r_{H_2} \cdot t \cdot N_A \quad \textbf{(Eq. 3.8a)}$$

$$N_\gamma = \frac{E\ total}{E\ photon} = \frac{I_{rad} \cdot S_{rad} \cdot t}{\frac{h \cdot c}{\lambda_{inc}}} \quad \textbf{(Eq. 3.8b)}$$

So:

$$AQY(\%) = \frac{2 \cdot r_{H_2} \cdot N_A \cdot h \cdot c}{I_{rad} \cdot S_{rad} \cdot \lambda_{inc}} \cdot 100 \quad \textbf{(Eq. 3.8)}$$

being r_{H_2} the hydrogen production rate from **Equation 3.6** (in mol/s), N_A the Avogadro's number ($6.022 \cdot 10^{23}$ molecules/mol), h the Planck's constant ($6.626 \cdot 10^{-34}$ J·s), c the speed of light ($3 \cdot 10^8$ m/s), I_{rad} the irradiance of the incident light (W/cm^2), S_{rad} the irradiation area (Having a 4 cm inner diameter, 12.57 cm^2) and λ_{inc} the wavelength of this incident light (nm = 10^{-9} m).

3.6. Sample Characterization

In order to obtain useful information about the photocatalytic samples and ensure the integrity of the P90 TiO_2 nanoparticles after the ball milling, two characterization techniques have been carried out on the samples: Raman spectroscopy for the study of the TiO_2 phases, Scanning Electron Microscopy with Energy Dispersive X-ray spectroscopy (SEM/EDX) for the imaging and sizing of the particles and spectrophotometry for measuring the light absorption of the samples.

3.6.1. Raman Spectroscopy

Raman spectroscopy is a non-destructive chemical analysis technique based on the inelastic scattering of monochromatic light, and consisting on the emission of photons with a (monochromatic) laser through a sample [38,39].

When the photons of the light are absorbed by the sample, in most cases energy of the molecule is unchanged after its interaction with the photons, so they are reemitted normally with the same energy and so wavelength, which is called elastic or Rayleigh scattering. However, in very few cases (0.0000001% of photons), an inelastic scattering called Raman occurs, in which the molecule gains or losses (Stokes or Anti-Stokes) energy from the photon, changing its wavelength when reemitted [38,39].

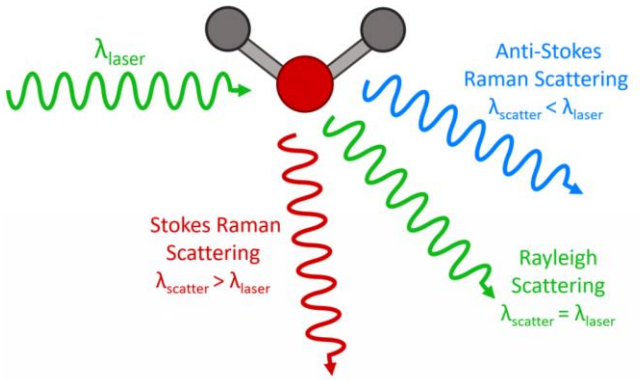

Figure 3.10. *Three types of scattering processes that can occur when light interacts with a molecule. (Source: EDINST* [38]*).*

Then, the equipment gathers the scattered light in a Raman spectrum, in which a number of peaks, showing the intensity and wavelength position of the Raman scattered light, are presented. Each peak corresponds to a specific molecular bond vibration, allowing this technique to identify substances through their characteristic Raman 'fingerprint'. So, Raman spectroscopy constitutes a very useful technique which can provide information about the chemical structure, phase and polymorphy, crystallinity and the presence of impurities [38,39].

As said before, this technique is a non-destructive, meaning that the sample used can be recovered after using it. Its preparation for the characterization process consisted only in the deposition of a small quantity of the powder over a metallic plate.

3.6.2. SEM/EDX

Scanning Electron Microscopy with Energy Dispersive X-ray spectroscopy (SEM/EDX) is the best known and most widely-used of the surface analytical techniques to study the morphology and elemental composition of a solid sample. High resolution images of surface topography, with excellent depth of field, are produced using a highly-focused, scanning (primary) electron beam [40].

Upon contact with the sample, the focused beam of electron will produce secondary electrons (SEs), backscattered electrons, and characteristic X-ray, which is then detected with respective detectors and finally displayed on the monitor. SEM image is formed with the signals of the low energy SEs emitted from the sample, whose intensity is dependent on the surface topography of the sample [41].

In the case of EDX spectroscopy, this technique is involved in the detection of elemental composition of substance by using scanning electron microscope. As mentioned before, in addition to low energy secondary electrons, backscattered electrons and X-rays are generated by primary electron bombardment. The intensity of backscattered electrons can be correlated to the atomic number of

the element within the sampling volume, while the characteristic X-ray emission spectrum of each element can be differentiated and measured for determining its concentration in the sample [41].

Contrary to the simple preparation on Raman spectroscopy, in this case the samples had to be poured onto a thin silicon plate, which was glued with a silver paste to a SEM sample holder, in order to ensure electrical conductivity through the sample that allow the electron bombing. Also, they could not be recovered after their use.

3.6.3. Spectrophotometry

Spectrophotometry is a standard and inexpensive technique to measure absorption or reflection of light by a sample over a certain wavelength. The equipment is composed of a spectrometer, which produces the desired light spectrum (changing the wavelength with time) and the photometer, which measures the intensity of light by measuring the amount of light that passes through the sample at each wavelength. This intensity is compared with a blank sample, assumed to have zero absorption of light [42].

The preparation of the sample for this technique has been again very simple, as the proper filter papers impregnated with the photocatalyst have been able to be introduced in the equipment.

4. CHAPTER 4: RESULTS AND DISCUSSION

This chapter describes the different experiments carried out and the results obtained. These experiments were divided into different sets, each of them with a different evaluation objective.

4.1. Set 1: Au, Ag, Cu Comparison

As discussed in the previous chapter, three different metals, gold (Au), silver (Ag) and copper (Cu), have been proposed as the 3rd metal to be loaded in the photocatalyst. These three metals have in common that they are able to develop a LSPR effect under visible light irradiation, thus giving the photocatalyst the ability to be active under this type of light. The primary objective of this work is then to determine if this effect is achieved by loading each metal to the TiO_2 with the ball milling technique from their saline precursors, together with the ones of Pd and Pt.

So, as a starting point of the experimental work, hydrogen production has been assessed changing the third metal of the TiO_2 / PdPt**Me** photocatalyst, where **Me** was chosen between Au, Ag and Cu, in order to select one of them for the further experiments. As stated before, 1.5 wt.% of total metal loading (35:35:30) has been chosen for these initial samples, and the experiments were performed with UV + visible light (no filter) and at a high irradiance value (105 mW/cm^2).

One powder sample for each metal has been synthesized by mechanochemistry using TiO_2 P90 as a photocatalytic supporting material, and a first round of experiments impregnating these powders right after synthesizing them has been performed, obtaining the following results:

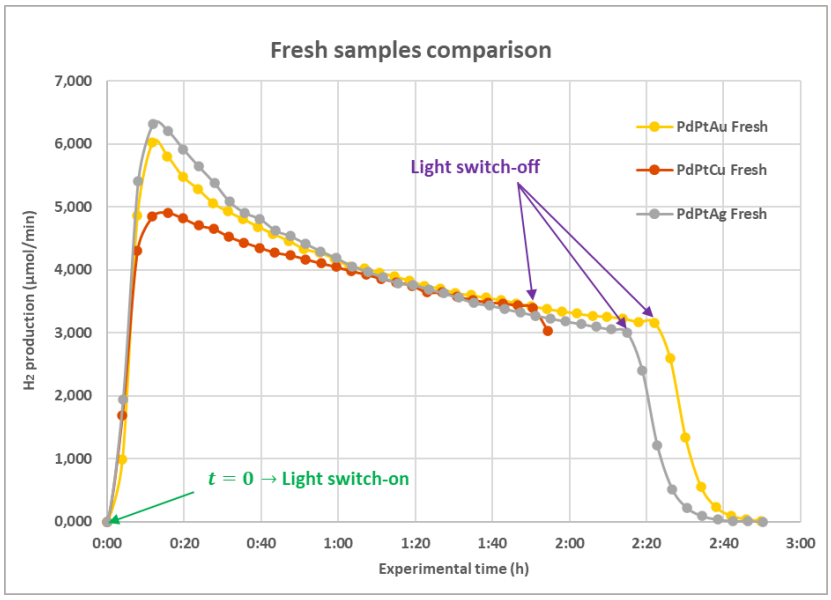

Figure 4.1. *H_2 production rate with time with fresh samples for the different TiO_2/PdPt**Me** combinations (1.5 wt.% total metal load, UV+Vis → I_{rad}=105 mW/cm^2)*

In these samples, a similar tendency on the evolution of the H_2 production rate was appreciated in all cases: a maximum peak of production is achieved right after turning the light on, and after that the production rate decreases, at first rapidly and then more slowly, tending to a more or less constant production rate. The reasons for this behaviour could be explained by the structure of the photocatalyst achieved with the ball milling technique mentioned in previous chapters: the local high temperature resulting from the mechanical energy of the impacts and friction between the grinding ball, bowl and the powder induces the decomposition of the metal salts, which causes the dispersion of the metal atoms over the surface of the TiO_2 nanoparticles, forming very small metallic clusters (of 1 nm or less) in which these metal are in a highly energetic state due to the excitement by the mechanical forces. These clusters, which show enhanced photocatalytic activity, tend to less and then more stable energetic states by aggregating to form larger particles, process that is favoured under thermal (particle diffusion/coalescence and Ostwald ripening) and/or light irradiation (still not fully interpreted) environments [37].

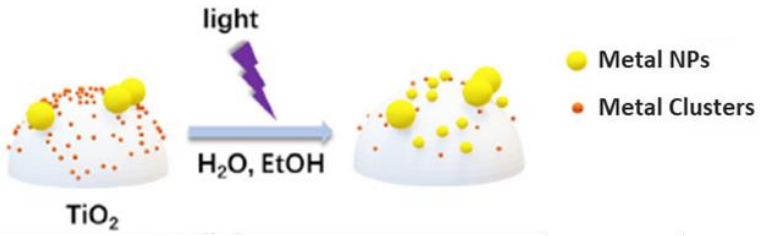

Figure 4.2. *Changes of metal species during the studied photoreaction of hydrogen generation* (Source: modification from Y. Chen [37]).

So, during the photoreaction process, the incident irradiation, together with the increase on temperature (especially due to the visible light), would induce this aggregation effect that result in the decrease on the photocatalytic activity of the particles and so the decrease in the hydrogen production rate until the disappearance of all these clusters. Additionally, the presence of ethanol molecules acting as electron donors and the UV light irradiation over the TiO_2 surface generates a reducing environment that could also promote the reorganization of metallic clusters into larger metallic nanoparticles.

Now, comparing the results of the three samples, while this final H_2 production rate was more or less similar for the three metals, the main difference lies on the maximum production rate achieved, similar in the case of Ag and Au (95 and 90% approximately higher than the final tendency of production rate) but quite lower in the case of Cu (around 50%).

A second round of experiments has been carried out with the same synthesized powders, in which the impregnations have been done one day after the synthesis, in order to assess the stability of the photocatalytic samples. Similar tendencies can be seen, but higher differences between the production rates are shown among them, as the overall decrease of the rates differs depending on

the sample. Cu, with the worst performance among the fresh samples, suffers a great decay that distances it from the other samples; between Ag and Au, the most promising ones, differences also increased due to a higher decay in case of the Au sample.

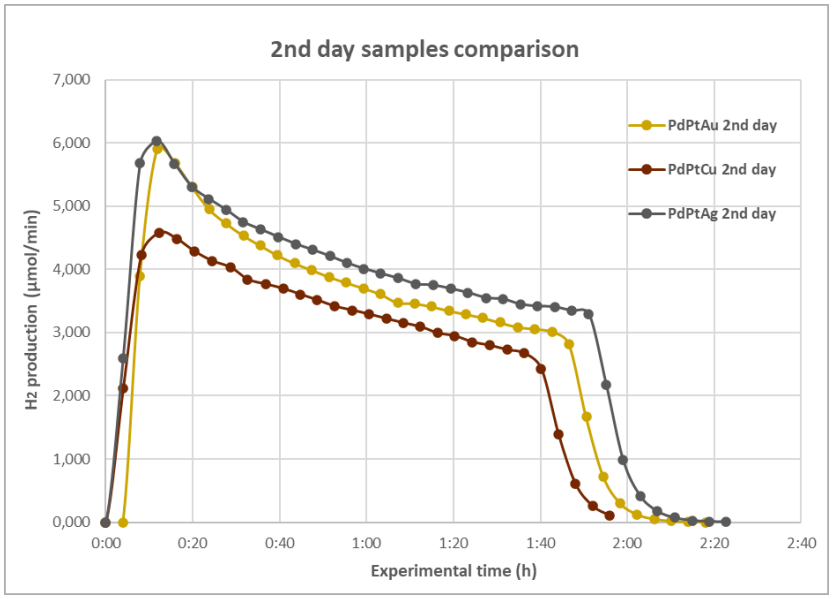

Figure 4.3. *H_2 production rate with time with 2nd day samples for the different TiO_2/PdPt**Me** combinations (1.5 wt.% total metal load, UV+Vis → I_{rad}=105 mW/cm^2).*

This decay between the fresh and the 2nd day samples can be more clearly seen with the individual graphical comparison of each of the metal samples (**Figure 4.3**). By this comparison it can be stated that the most stable sample that does not suffer an important decay is the silver sample, showing a very similar H_2 evolution profile on both photocatalytic experiments.

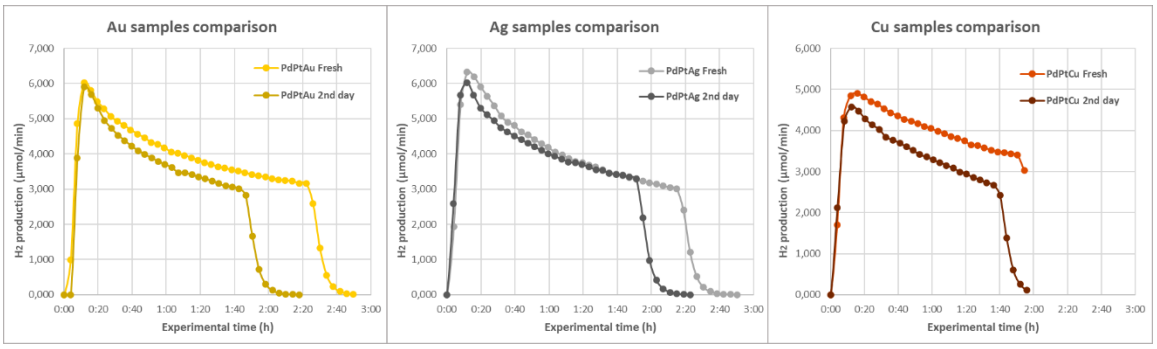

Figure 4.4. *Comparison of H_2 production rate with time between fresh and 2nd day samples for each TiO_2/PdPt**Me** combination (1.5 wt.% total metal load, UV+Vis → I_{rad}=105 mW/cm^2).*

This change in the production rates can be related to an aging process of the samples under atmospheric conditions, as changes in the colour of gold (from grey to green) and copper (from a greenish grey to white) powders were noticed the day after synthesizing them, despite they were

stored minimizing the contact with light. Nevertheless, in the case of the silver powder, this colour change was no observed (both fresh and aged samples kept a yellowish shade).

Figure 4.5. *From left to right, fresh (above) and 2nd (below) TiO_2/PdPt**Me** powders with Au, Ag and Cu.*

This could be explained again by the supported metal structures: when the metal precursors underwent a high energy mechanochemical process to form high reactive catalytic clusters, they can show different oxidation states, which were no present in the original metal salt, so this change in colours could be attributed to the exposure to air (with O_2 as an oxidizing agent and N_2 as a reducing agent) and light that would induce either slow changes on these oxidation states and/or the aggregation/reorganization of the metallic species of the clusters, decreasing the initial photocatalytic activity of the sample with the time.

Therefore, in view of the obtained results, silver has been chosen as the third metal to load on the photocatalyst in the further experiments of this study, not only because of showing the best performance among the three metals, but also because of the good stability of the obtained powder, which confers more flexibility to the experimental work by not being forced to synthesize the fresh photocatalytic sample just before the H_2 evolution experiments, as well as by allowing to use the same powder several days in case of being necessary. Also, Au, with a not much worse performance, has been previously reported in several experimental works (alone or with Pt, never as 3rd metal) [22,26,35], so a new approach with a different metal has been decided to be adopted for this work, encouraged by the lower cost of silver in front of the gold, with the aim of reducing the production cost of the photocatalyst (the amounts of noble metals Pd and Pt will be also optimized in an attempt to reduce the costs without losing a significant photocatalytic performance).

4.2. Set 2: Synthesis order comparison

Once chosen Ag as **Me** in the TiO_2/PdPt**Me** photocatalyst, a series of experiments about the ball milling synthesis have been performed. As the influence of the main parameters (ball-to-powder ratio, time and frequency) has been reported in previous works [35,37], the object of study in this work has been whether loading the metals non-simultaneously and in different orders had some influence in the hydrogen production.

To do so, different samples (keeping an overall metal loading of 1.5 wt.%) were prepared with the different synthesis orders: one loading Pd and Pt with TiO_2 on a first ball milling round, and loading then Ag on a second one, and the other one loading Ag on the first round and Pd + Pt on the second one. As been the ball milling round maintained at 10 min, apart from the original sample (the one from previous set), a second powder with simultaneous loading of the three metals but on a unique round of 20 min instead has also been synthesized to perform more fair comparisons. Again, this set of experiments has been performed with UV + visible light (no filter) but with a lower irradiance value (85 mW/cm^2). This new value of irradiance has been decided due to the high increase in the temperature with the previously used value (see **Annex B**), that could compromise the stability of the sample and accelerate the cluster aggregation, and to operate at a more similar value than previous works performed by the research group, for better comparison [37]. Results are shown below:

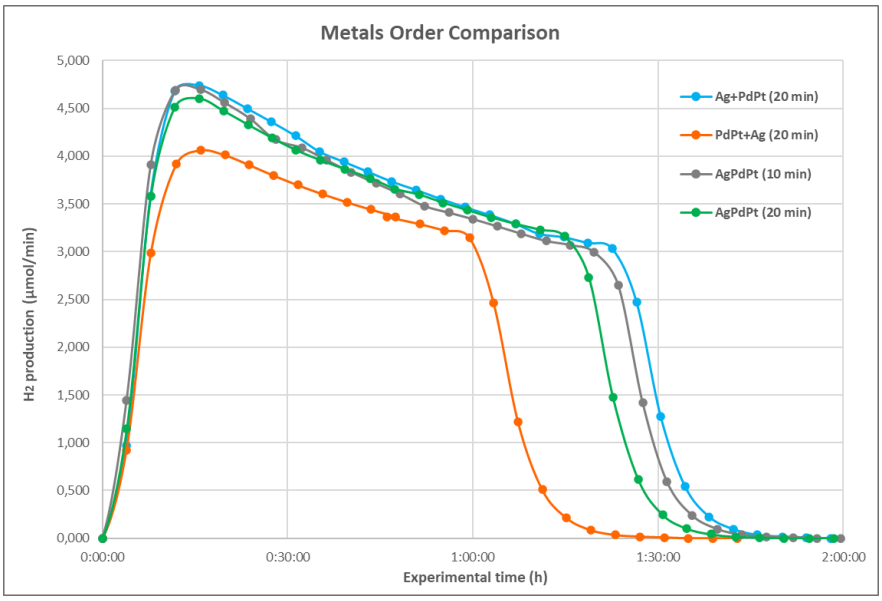

Figure 4.6. *H_2 production rate with time by TiO_2/PdPtAg samples with metals order variation synthesis (1.5 wt.% total metal load, UV+Vis → I_{rad}=85 mW/cm^2).*

Considering all the H_2 evolution curves of all the samples in **Figure 4.6**, the obtained results are very similar, the only little difference can be found in the one with the loading divided into Pd + Pt (1^{st}) and Ag (2^{nd}). This decrease in the production could be related to the reorganization (probably agglomeration) of metal particles and the formation of defects due to an excessive time subjected to mechanical stresses, as previously commented [35]. However, in the reverse order sample and the simultaneous 20 min one, this H_2 evolution rate decrease is not observed at all, so probably the differences would only be due to experimental errors (e.g., photocatalyst losses during impregnation, light intensity variation). Therefore, it can be concluded that the order in the synthesis of metals do not imply important changes in the photocatalytic activity, and further synthesis combinations (3 rounds, each one with one metal, and in different orders) were discarded.

4.3. Set 3: Metal proportions comparisons

After analysing the effects on varying the non-studied [35,37] ball milling synthesis parameters and tunning them, the experimental work has been focused again on determining the composition of the photocatalyst that could achieve the highest hydrogen production rate. As silver was previously chosen as the third metal, now the object of study has been to explore the ratios in which the three metals are loaded.

As mentioned before, the quantities of metal salts to be weighted restrict the possible proportions of study due to the sensibility of the available scale in the laboratory. As the quantity of Ag salt was near the limit (especially when intending to reduce the total % of load in subsequent experiments), and as being the main object of study (analyse the SPR effect), we decided to increase its proportion while lowering those of Pd and Pt, which were always in equal amounts. This decision was also motivated due to economic reasons, since Pd and Pt salts represents the most important part of the price of the photocatalyst (see **Chapter 7**), so reducing the proportions of these two compounds would decrease its price sharply.

This increase in the proportion of Ag was again limited by the quantities of Pd an Pt salts that we were able to weight on the scale. Attending on this limitation, two samples have been prepared: one sample near the minimum acceptable quantity of salts, in this case 70% of Ag (15% of Pd/Pt), and other sample between this maximum Ag proportion and the original one of 30%, so 50% of Ag (25% of Pd/Pt). Respect to the total metal loading, it has been maintained at 1.5 wt.%, as in the previous experiments. Below are shown the new salt quantities used:

Table 4-1. *Required quantities of TiO_2 and metal salt powder for each of the metal proportions (Total metal load = 1.5 wt.%).*

	Ag	Pd/Pt	Ag salt	Pt salt	Pd salt	TiO_2
Original	**30%**	**35%**	0,0026 g	0,0040 g	0,0041 g	0,3624 g
Intermediate	**50%**	**25%**	0,0044 g	0,0028 g	0,0029 g	
Maximum	**70%**	**15%**	0,0061 g	0,0017 g	0,0017 g	

The experiments were performed again with UV + visible light (no filter) and with the same irradiance than in the previous set (85 mW/cm^2). The results obtained for these two samples, including the those of the original sample, are presented in the following graph:

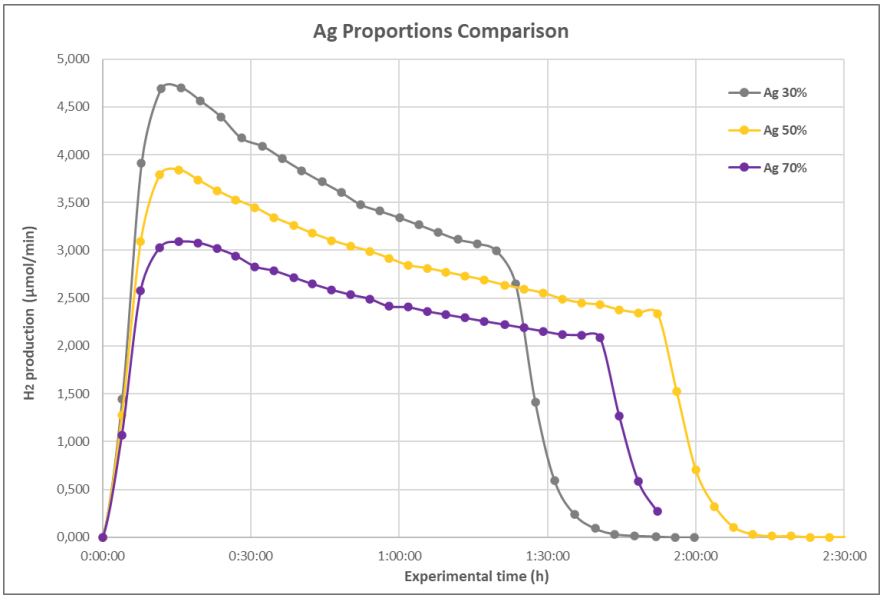

Figure 4.7. *H_2 production rate with time by TiO_2/PdPtAg samples with different proportions of Ag (1.5 wt.% total metal load, UV+Vis → I_{rad}=85 mW/cm^2).*

As it can be observed, the overall H_2 production rate decreases with the increase of the Ag proportion, and even the maximum peak is more accentuated with lower proportions of it. This decrease shows that despite having assumed this peak as the enhance of production under visible light due to the SPR effect achieved with presence of Ag species (hypothesis that will be reinforced by the results obtained in the next set of experiments), this would be limited by the presence and concentration of the Pd and Pt metals in the sample. As has been mentioned before, these noble metals are expected to act as the active sites of the reduction reaction, as the nucleation of hydrogen over them acting as cocatalysts presents a lower overpotential than over TiO_2. Moreover, interactions between Pd/ Pt and TiO_2 are also crucial for the efficient charge carrier transfer between the TiO_2 conduction band and the Fermi level of the metals, enhancing the electron–hole lifetime by means of the created Schottky barrier [43]. Then, which could happen is that, despite the generation of a higher quantity of hot electrons by the SPR effect, the lower amount of Pd and Pt would reduce the quantity of available active sites that promote the H_2 evolution, so most of these electrons would recombine without being able to participate in the photocatalytic redox reaction. Another reason to that would be that, with the increase in quantity of Ag, the distribution of the metals atoms in the clusters would result in the partial coverage of the Pd and Pt fraction by the Ag fraction, neglecting them to participate in the photocatalytic activity. Anyway, results clearly indicate that the overall photocatalytic activity, and probably the one under the visible fraction of light with the Ag, is limited by the amount of Pd and/or Pt present in the samples, so proportions were kept as the initially proposed ones (35:35:30 Pd:Pt:Ag) for further performed experiments.

4.4. Set 4: Co-catalyst Loading and UV/Visible Comparison

Once determined the right proportions of the metals, the only pending issue regarding the photocatalyst composition is the assessment of the total metal co-catalyst loading. Then, the original 1.5 wt.% loaded sample was decided to be compared with 1 wt.%, stated as the best load % in previous experiences with monometallic co-catalysts [22], and also with a 2 wt.% load. Again, samples with loads below 1 wt.% were not possible to be prepared due to the measuring of the salts in the scale.

In this set of experiments, the evaluation of the production of hydrogen comparing UV and visible light has also been performed, in order to evaluate the possible SPR effect caused by the Ag particles. To do so, each experiment comprises a first step with UV + Visible light, as in the previous ones, and a second step with only UV light, for which the filter is needed to be installed in the LC8 light source. Both stages have been performed at the same value of irradiance (85 mW/cm^2), so also the intensity of the light source was tuned between stages according to **Figure 3.6**. Also, as the visible light is the main responsible for the increasing of temperature (see **Annex B**), an external heating source has been used (a hot air gun) when using only UV light to have similar temperature conditions in both steps of the experiments, and so more fair comparisons. Below are shown the results obtained with the three samples:

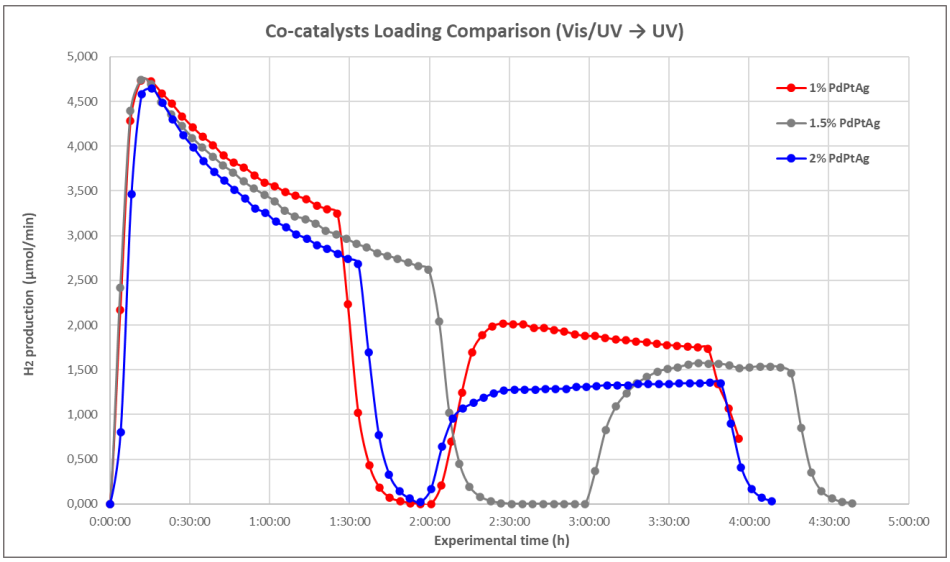

Figure 4.8. *H_2 production rate with time by TiO_2/PdPtAg samples with different co-catalyst total load % and with Vis/UV (no filter) and UV (filter) steps (I_{rad}=85 mW/cm^2).*

From these results, high differences between the productions with only UV respect to UV + Visible light are observed, which would indicate a high contribution of the visible light on hydrogen production. What is also important to remark from these results is that equal maximum production peaks were obtained for the three percentages of metal load, and even the lower load sample, the 1

wt.% one, showed the slowest decay in the production with time (showing the 2 wt.% load the faster one). Moreover, in the case of the productions under only UV irradiation, production values with 1 wt.% load were again the highest ones.

Back to the comparison between UV + Visible and only UV irradiation, while the usual decay was observed in the first step, productions on the second one was more or less flat, which could indicate that the cluster reorganization (usually agglomeration of metallic species into bigger nanoparticles), concluded reason of the production decay, occur at much lower ratios when only UV light is irradiated to the sample. So, in order to perform further comparisons, the inverse order of steps, first UV and then UV + Visible has been also performed, with the object of evaluate the production under UV irradiation over the fresh samples.

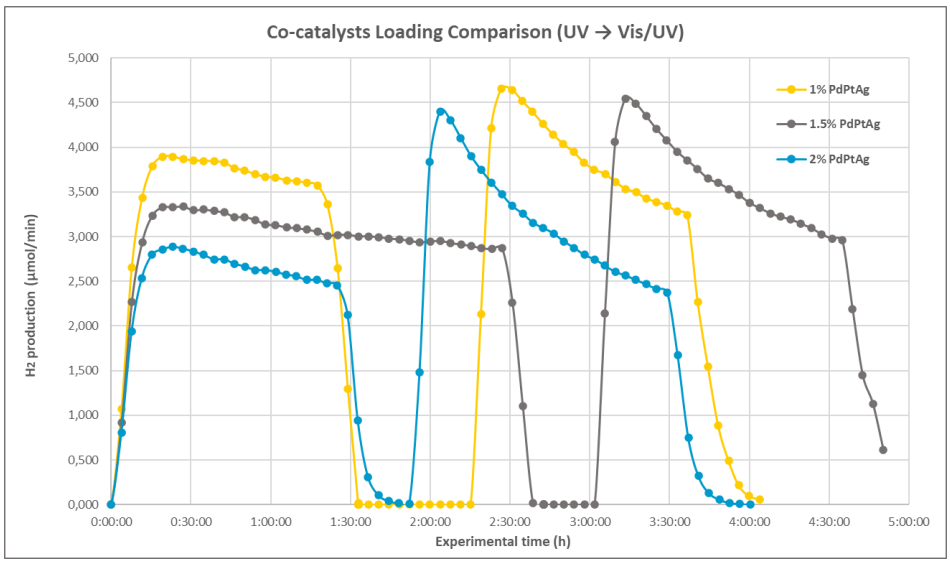

Figure 4.9. *H_2 production rate with time by TiO_2/PdPtAg samples with different co-catalyst total load % and with UV (filter) and Vis/UV (no filter) steps (I_{rad}=85 mW/cm^2).*

With this second set or results, it can be seen that the production differences between steps are not so big as the one obtained in the previous one. In this case productions with UV light are much higher than before, and also with very low decay rates, which would confirm the lower agglomeration of clusters under this type of irradiation (although the temperature is equal in both steps). This assumption is reinforced by the fact that the productions achieved in the second step of UV + Visible irradiation are almost equal than in the inverse order of steps (only a bit lower). Differences between orders are better appreciated with the individual comparisons for each loading %:

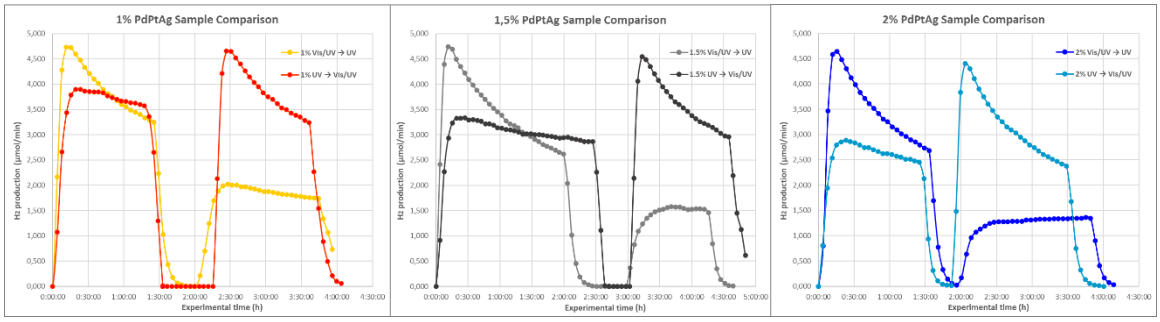

Figure 4.10. *H_2 production rate with time comparison between Vis/UV → UV and UV → Vis/UV tests for each co-catalyst total load % of TiO_2/PdPtAg samples (I_{rad}=85 mW/cm^2).*

In these comparisons shown in **Figure 4.10**, it can be seen that the final tendency production after decay with UV+ Visible light is very similar to the more or less constant value of production under UV light; this could indicate that the initial maximum peak would be primarily due to the LSPR effect of Ag under the visible fraction of the irradiation, effect that would disappear due to the rapid reorganization of the Ag cluster, while in the case of Pd and Pt this reorganization would either occur at lower rates or would have a smaller effect on photocatalytic activity of these metals (as for the SPR effect, the particle size is a very important factor to show it or not).

As explained in the previous chapter, in order to confirm the occurrence of the SPR effect on the samples, spectrophotometry tests were performed with the samples, in order to measure the absorbance of light by the samples as a function of its wavelength (actually the equipment used measured the reflection, being the translation to absorption a simple calculation). The 2 wt.% loaded samples were chosen for this test, as being the ones with more quantity of co-catalyst, and four different samples were compared: a fresh unreacted sample, a sample exposed to the UV + Visible and UV steps (in this order), another to the UV and UV + Visible steps and a final one exposed only to the UV step.

Figure 4.11 shows the results of these tests. In all samples an absorbance above to 90% is reached below wavelengths of approximate 365 nm (UV fraction of light), which corresponds to photon energies above 3.2 eV, the band gap of the TiO_2 (anatase phase) showed in **Figure 2.2**, denoting the region in which this semiconductor is photocatalytically active by itself. The range between 400 and 365 nm also experiments a high increase of the absorption in all samples (from 60 to 90%), being this the limit range in which the TiO_2 starts to be active (energies between 3-3.4 eV, being 3 eV the band gap of the rutile phase). Now, looking at the fresh sample, while in the upper range of visible light (>550 nm) absorption is very poor (below 30%), it experiences a sudden increase of absorption from 550 to 400 nm (from 30 to 60%). Looking into previous reports [44], this range corresponds to the one at which Ag nanoparticles show surface plasmon effect, confirming then the occurrence of this effect in the fresh samples.

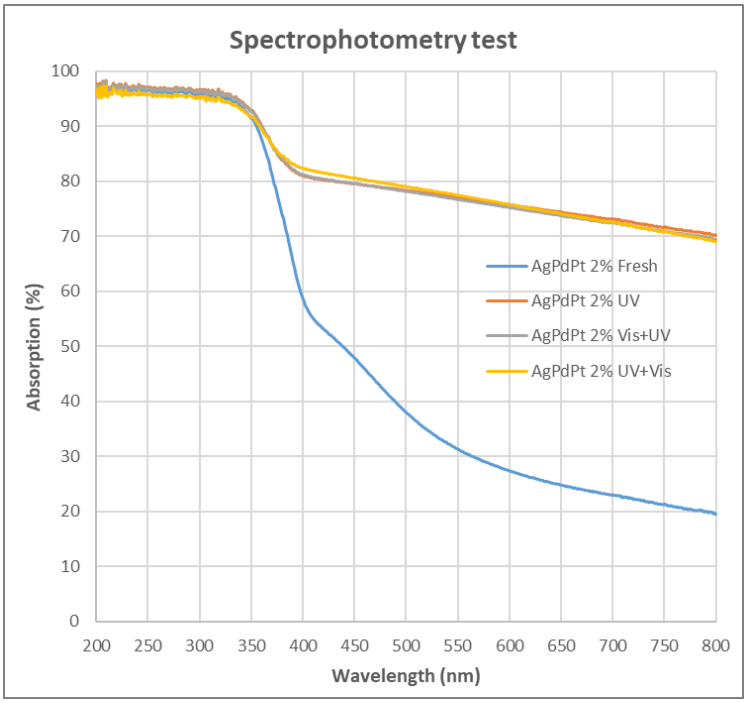

Figure 4.11. *Results of the spectrophotometry tests for the different samples of 2 wt.% total metal load.*

Compared to it, the absorption rate of light of the reacted samples did not experiment any change with the decrease in wavelength until the 400 nm of TiO_2, which may be an indicative of the disappearance of this effect due to the reorganization of the metallic clusters. In the reacted sample only prepared with UV, however, this effect was also expected to be still observed (what does not happen), as from the reaction experiments it was concluded that this exposure did not affect so much the activity of the sample in the next UV + Visible step. So, the reason of this flat absorption values in the visible range, which are in fact higher than in the fresh sample (around 70-80%), could be better attributed to the change (**Figure 4.12**) between a light colour in the fresh sample to a black colour in the reacted samples, which is due to the exposure to the light and the reducing environment inside the reactor (as being black, it absorbs all the visible light spectrum, but that does not mean a higher generation charge carriers and photocatalytic activity).

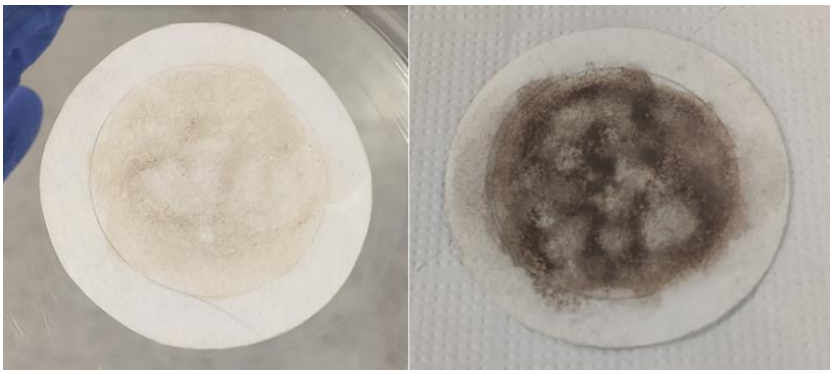

Figure 4.12. *Comparison between TiO_2 / AgPdPt samples before (left) and after (right) reaction.*

4.5. Extra set: Light intermittency

Looking into the hydrogen production decay with time due to the exposure of visible light, an extra test has been carried out, motivated by works that study the enhance of the photocatalytic activity when continuously switching on and off the incident light, subjecting the sample to intermittent light pulses [45,46]. So, an extra test has been decided to be done, in order to evaluate whether, by interrupting the irradiation of the sample, a recovery respect to the hydrogen production rate decay is achieved, either the initial maximum peak or an intermediate value. To do so, the chosen sample of 1 wt.% of total metal co-catalyst load with Ag being the 30% of it, has been subjected to a new experimental run, in which the light would be switched on and off at time intervals to check whether, when switching off and on again, the production experiments an upgrade. However, the results of the first cycle, seen in **Figure 4.13**, showed that the production started from the same point where the light was turned off. Then, from this experience it can be concluded, as also the previous tests indicate, that the activity of the catalyst is permanently affected by the exposure to visible light, suffering a decrease due to the irreversible reorganization of the metal clusters.

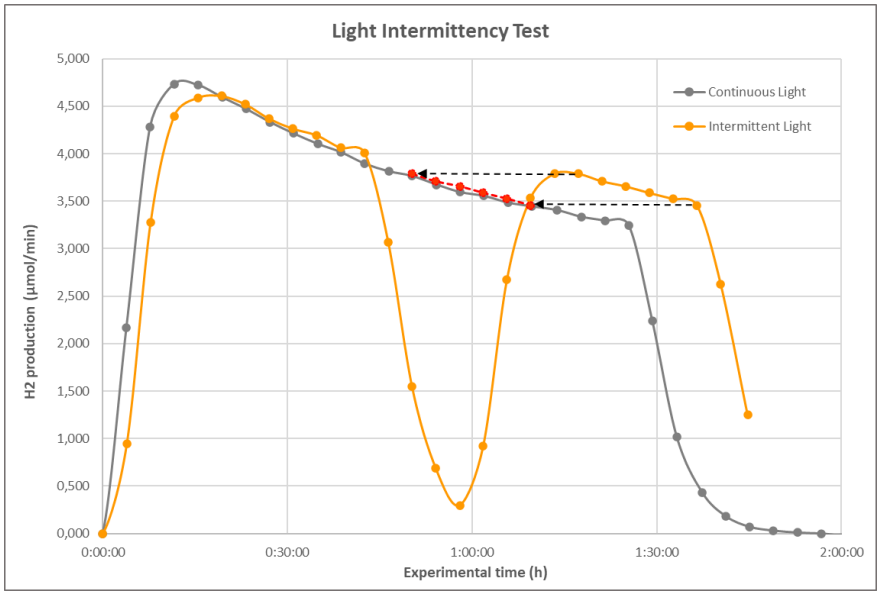

Figure 4.13. *H_2 production rate with time comparison between continuous and intermittent light incidence (1 wt.% PdPtAg, 30% Ag 35% Pd 35% Pt, UV+Vis → I_{rad}=85 mW/cm^2).*

4.6. Chosen Sample Results

As has been already said in the light intermittency test, the chosen sample with the most promising performance amongst the tested ones has been the one containing 1 wt.% of AgPdPt co-catalysts, with Ag in a 30% proportion and Pd/Pt in 35%. This sample showed the best performance both with UV + Visible light, with the lowest decay in the production rate, and with only the UV light, with the

highest production rate. In order to compare it with previous reports and experiments of the NEMEN group, the photocatalyst mass-dependant production rate of H_2 (in mmol/[h·g]) and the Apparent Quantum Yield (AQY, %) have been also calculated from the experimental data:

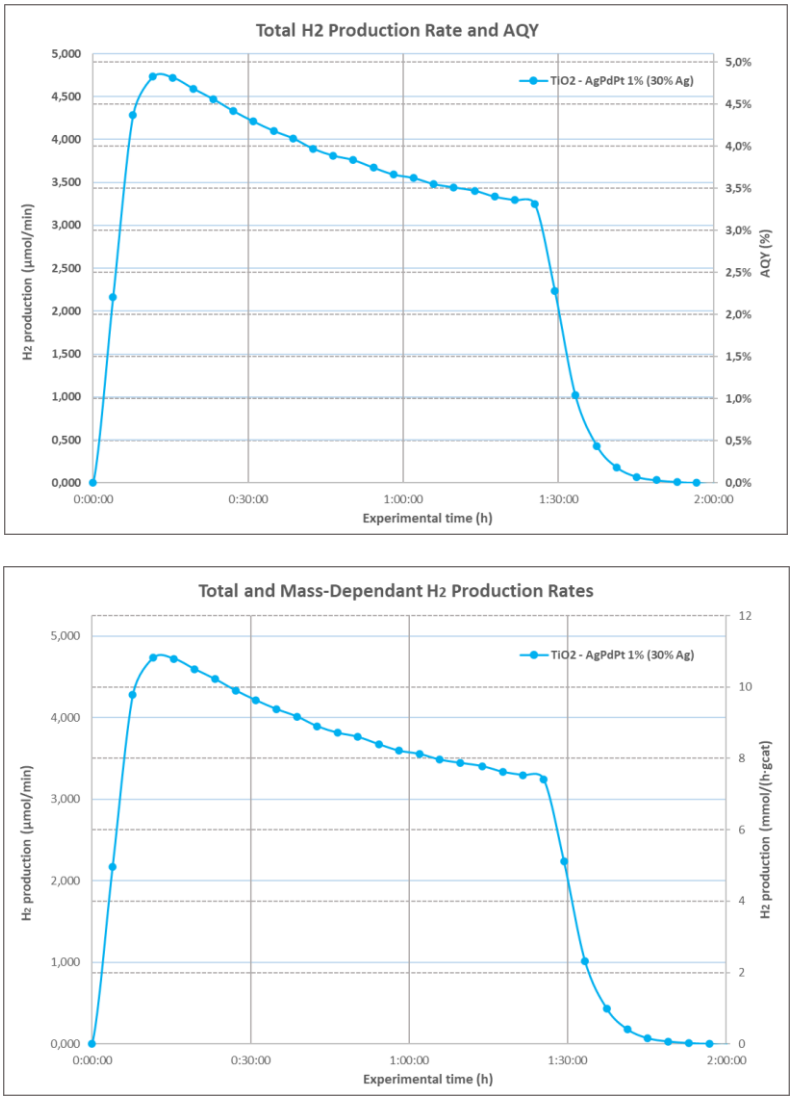

Figure 4.14. *Production performance parameters obtained from the experimental data of the chosen sample.*

Looking into the mmol/(h·g_{cat}) of H_2 produced, the obtained values show a better performance for the proposed trimetallic co-catalyst than for monometallic ones of Au or Pt [35,47] and also Au-Pt bimetallic ones [48] reported in previous reports under similar experimental conditions (irradiance and load %). Moreover, looking into the AQY, despite being the maximum 5% value far from the 10% marked as the initial starting point for practical application [11], is a very promising value near the maximum ones obtained in the present with very complex and expensive photocatalysts [11]. However, this comparison is not very accurate, as the 10% stated value corresponds to AQY referred to only visible light irradiance. In the present work, the available radiation monitor was only able to measure the irradiance around 365 nm UV light, value that has been used as reference in the

experiments and for the calculation of the AQY. It would be needed another instrument able to measure the irradiance value of the visible light range, unknown in our case, for a fairer comparison.

For a deeper study of the process, the obtained production rates of by-products were also quantified. As it can be seen in **Figure 4.15**, acetaldehyde was the main obtained by-product. Following stoichiometry of the main reaction of the process (**Equation 2.2**), its production should be equal to that of H_2, but as explained before, this substance is subsequently oxidized in secondary chain reactions, partly decomposing in other minor oxidation by-products. As can be seen in the figure, the ones detected by the GC, in descending order by amount produced, were CH_4, C_3H_8, CO_2, methanol, C_2H_6, Acetone and C_2H_4. Most of them, and also the order, are the typical ones for ethanol photoreforming processes, according to the literature [21], confirming then the assumed reaction pathway in which the hydrogen is produced by ethanol dehydrogenation. Looking into the UV steps and other samples, the same compounds were detected in similar proportions, confirming the veracity of the presented results.

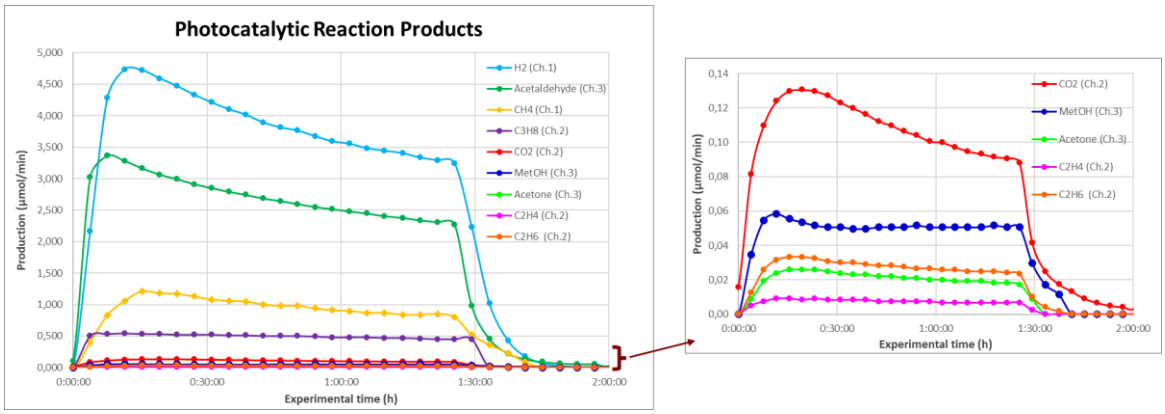

Figure 4.15. *Detected reaction products in the GC for the chosen sample (TiO_2 - AgPdPt 1 wt.%, 30% Ag).*

4.7. Photocatalyst characterization

In this final section, the obtained results from the characterization techniques are presented and compared.

4.7.1. Raman Spectroscopy

In the present work, the object of study with this technique has been the recognition of the different phases of TiO_2, anatase and rutile, on the photocatalyst, comparing the TiO_2 fresh powder with the prepared powder of photocatalyst to see whether the phases suffered modifications with the ball milling technique. Here can be seen the spectrum obtained for both cases:

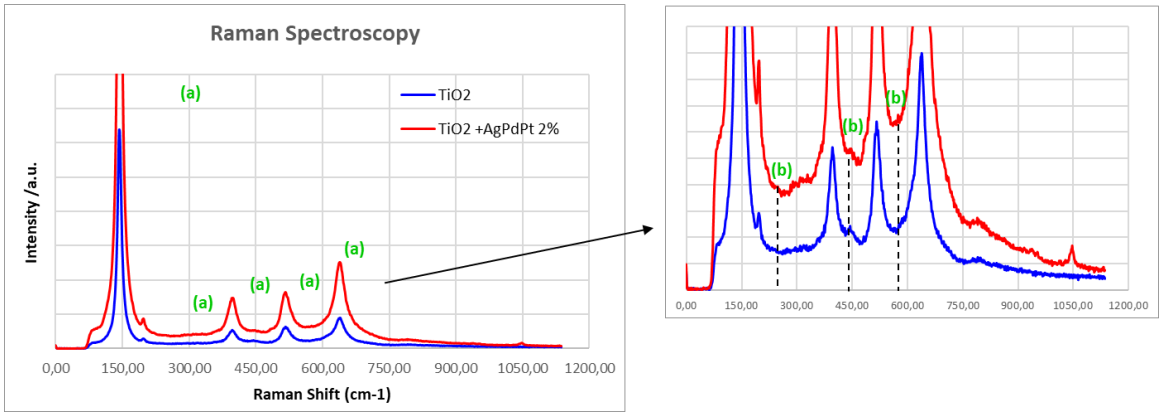

Figure 4.16. *Obtained spectrums with the Raman spectroscopy characterization.*

The most visible bands at around 150, 200, 400, 525, and 650 cm^{-1} (a) are characteristic of the anatase phase of TiO_2, while very small ones can be also distinguished at around 200, 450 and 600 cm^{-1} (b), which correspond to the small percentage of rutile phase present in commercial TiO_2 P90 [49,50]. The importance of these spectrums is that these band can be seen in both of them with the same change (taking into account the difference in the plotted overall intensity), showing that the TiO_2 phases stays unchanged after ball milling. The only difference that has been observed was an extra peak at around 1050 cm^{-1} in the prepared powder (c), which is attributed to the TiO_2 "impurities", probably the anions of the metal salts (nitrate, acetate or acetylacetonate) or even the Ag, able in some case of showing signal in this technique [51].

4.7.2. SEM / EDX

As explained before, the purpose of this technique has been again to compare a sample of fresh TiO_2 with a sample of prepared photocatalytic powder with ball milling. With the SEM images, the intention has been to check if the TiO_2 nanoparticles stay with a similar size after the ball milling, and also to check if co-catalyst clusters are appreciated, although it is not expected a priori due to their low concentration of the metals. The EDX spectrum has been recorded as an extra, to see if the quantities of these metals are sufficient to be detected.

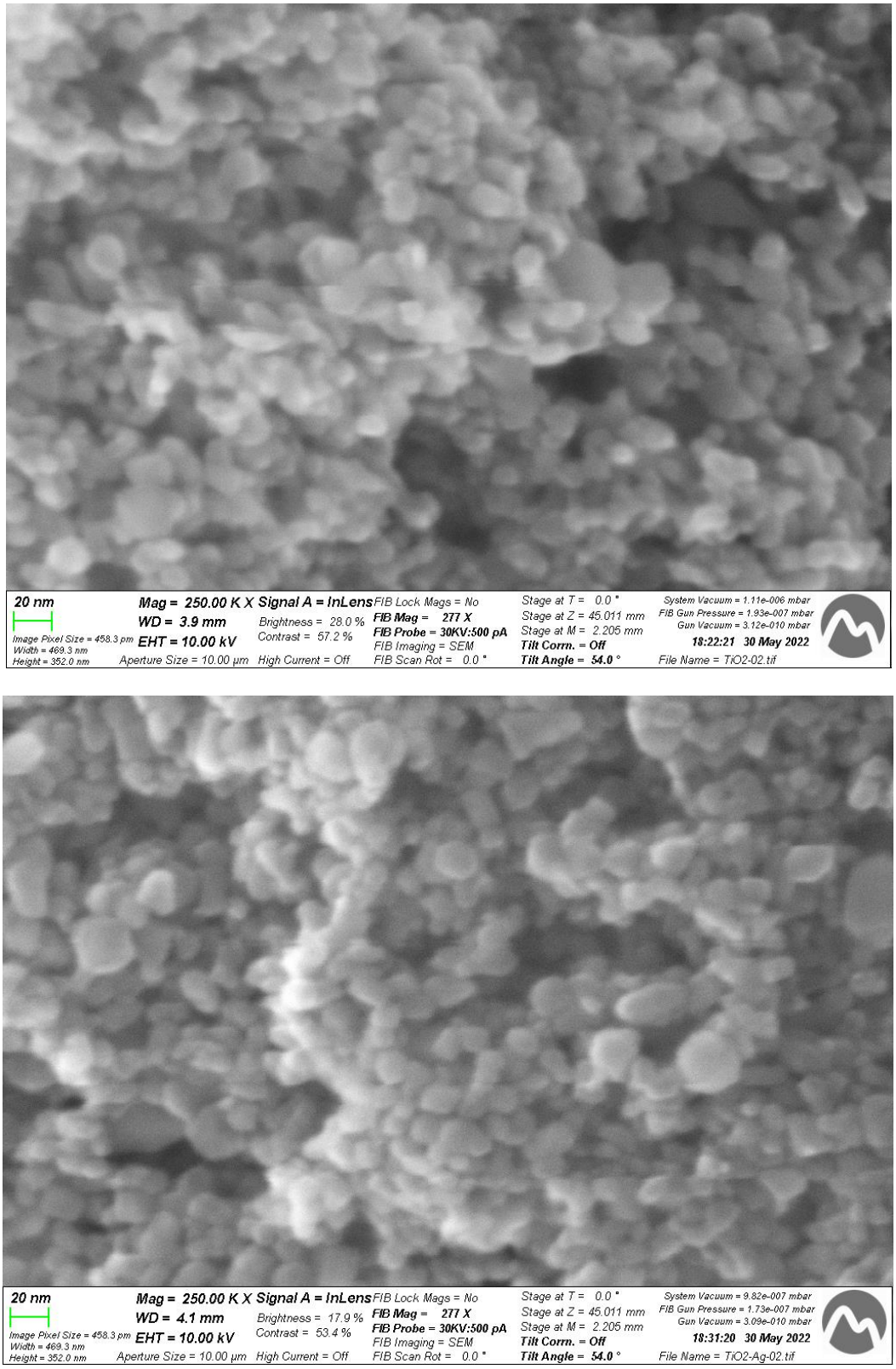

Figure 4.17. *SEM images of the Fresh TiO_2 sample (above) and the ball milled photocatalytic powder (2 wt.% AgPdPt) (below).*

Figure 4.17 shows the SEM images for both samples. It can be seen that, in both cases, most particle size ranges between 10 and 20 nm, with some bigger particles, but in general it can be stated that the ball milling did not affect the particle size distribution. This was confirmed by manually measuring these particles with FIJI ImageJ software, obtaining similar size distributions:

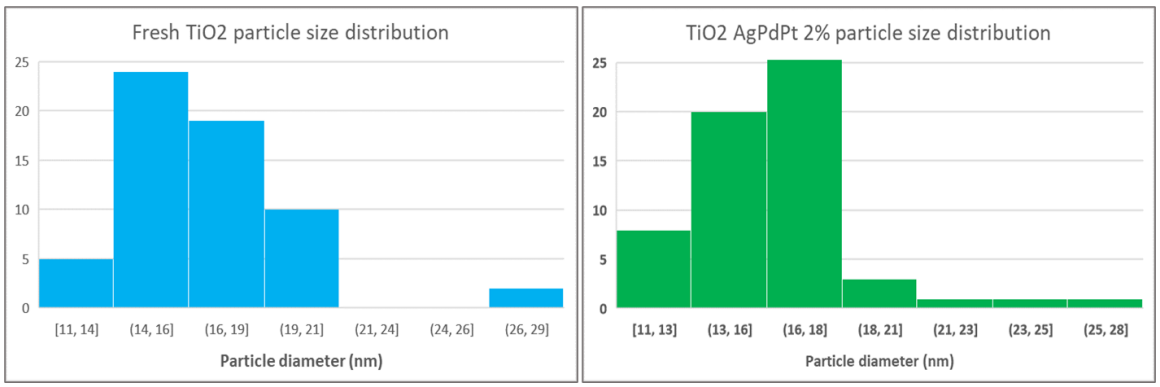

Figure 4.18. *Histograms of particle size distribution of the Fresh TiO_2 sample (above) and the ball milled photocatalytic powder (2 wt.% AgPdPt) (below).*

On the other hand, as expected due to their low concentration, no distinction was observed in the image about the presence of the metal clusters. Then, its presence, although barely detected, has been confirmed by the recorded EDX spectrum:

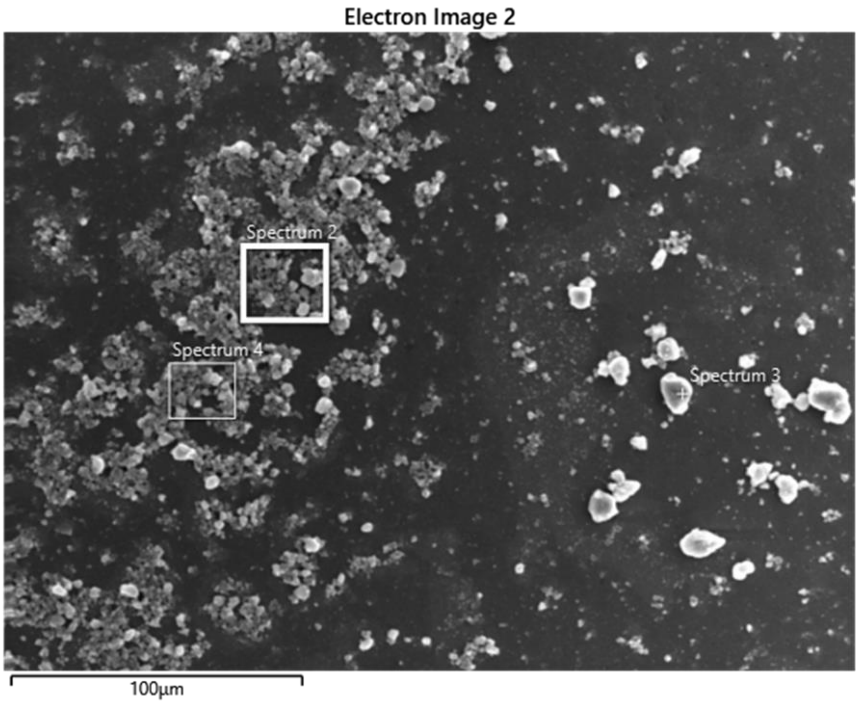

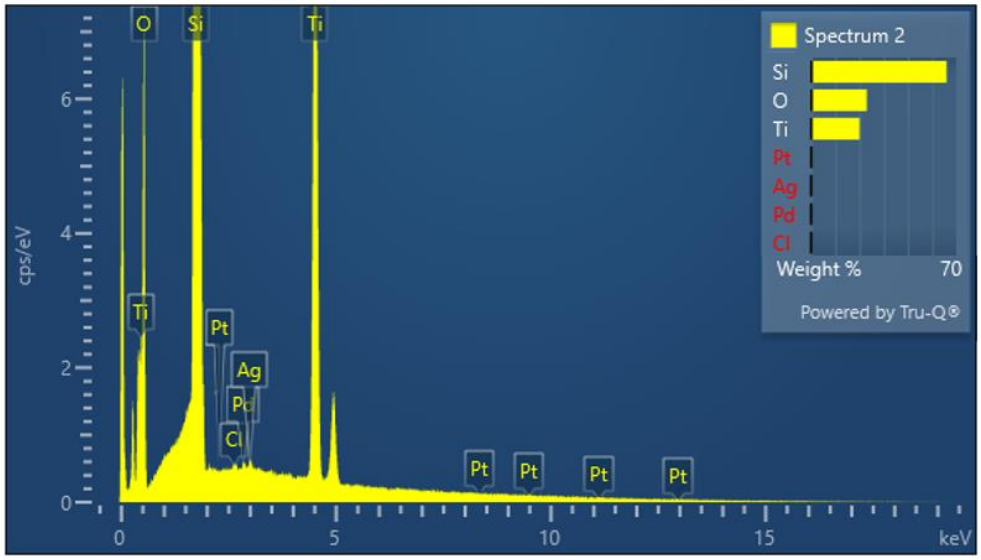

Figure 4.19. *Sample areas of recorded EDX spectrums (above) and results of one of them (below).*

5. CHAPTER 5: CONCLUSIONS

In the present project, the effect of trimetallic mixtures acting as co-catalysts on the enhance of the photocatalytic activity of TiO_2 for H_2 production from H_2O + EtOH 9:1 gaseous mixtures under UV and visible light, has been studied. To do so, a specifically designed experimental set-up for the development of the experiments under UV + visible light irradiation has been constructed. The tubular photocatalytic reactor coupled to a solar simulator lamp has been demonstrated as a feasible set up to perform heterogeneous solid-gas photocatalytic reactions under continuous mode.

The mechanochemical synthesis to load multiple metals onto the surface of commercial P90 TiO_2 support nanoparticles employing a ball milling equipment has been demonstrated as a very easy and efficient technique to form very small and highly active photocatalysts formed by multimetallic nanoclusters over the TiO_2.

The characterization of the samples by Raman spectroscopy and SEM/EDX showed no changes in the particle size of the TiO_2 before and after the mechanochemical treatment and also in the predominant anatase phase, and also confirm the presence of the metals in the particles. However, due to the SEM limitations in the resolution of subnano objects at high magnifications, the clusters size and structure, as well as the oxidation state of the metals on them, were not possible to study due to time limitation of a master thesis and availability of the analytical instruments.

Several comparisons between samples with different metal combinations, quantities or synthesis parameters were studied, in order to choose the one with the better performance.

From the results obtained, Ag was chosen as the 3rd metal, being its samples the ones with better performance and stability, when combined with Pd and Pt. Whereas the multimetallic clusters were successfully mechanochemically anchored onto the TiO_2 surface, the results of the photocatalytic experiments also showed a decrease of the H_2 production from an initial maximum peak with time, which suggested the reorganization of the metallic clusters during the photocatalytic reactions, obtaining less active particles due to the temperature and incidence of light on them. The reorganization was demonstrated to deactivate more the multimetallic species when UV+vis light were both together irradiating the sample. This higher deactivation under UV+vis irradiation suggests that the photocatalysts prepared during this work have to be improved before using them for practical applications.

The synthesis by simultaneous or staggered addition of the metals during the ball-milling was compared. Similar performance results were obtained, maintaining the initial decision of simultaneous load as being the fastest one.

After that, raise the proportion of Ag in the sample in front of the other two metals was studied. However, results showed the better performance with the initially proposed 30%. From these results it can be assumed that the enhancement of photocatalytic activity and response to visible light achieved with Ag is limited to the presence of the other two metals.

Finally, performances with 1, 1.5 and 2 wt.% of total load of metals were compared, and the results showed that the effect of aggregation was mainly due to the visible light exposure, as during UV steps production stayed constant. Also, it was observed that UV productions were very similar to the final tendency of the UV + Visible steps, which could suggest that the difference between these productions and the initial maximum peaks in the UV + Visible steps represents the enhance achieved with the visible light by the LSPR effect of Ag, and so that the reorganization of the clusters especially affects the activity of this metal.

From this last round of experiments, the sample with the best performance, the one of 1 wt.% load, was also determined. A maximum production rate under UV + Visible light of almost 5 μmol/min (11 mmol/[h·g_{cat}]) was obtained, a better value than previous samples with monometallic co-catalysts. Also, a maximum AQY of nearly 5% was obtained. These AQY values are promising and pave the way to perform more research in multimetallic clusters anchored onto a photocatalytic semiconductor material.

6. CHAPTER 6: FUTURE PROSPECTS

As stated before, this project constitutes the starting point in the NEMEN group for further research about trimetallic mixtures acting as co-catalysts over a TiO_2 photocatalyst. Then, the information extracted from the results obtained and the experience gained during the construction of the experimental set-up and the performance of the experiments should be taken into account for the development of future works.

Following our own experience so far, the following approaches are proposed for a deeper study in this research line:

- With the adequate equipment, more modifications on the sample should be compared (e.g., decreasing more the quantity of Ag with an adequate scale) and also the effect of visible light on the production should be quantified correctly (e.g., by using equipment able to measure the irradiation on this range and using a filter for the light source able to isolate this range instead of the UV range).
- For the same samples, a study on the evolution of the H_2 production by changing the incident irradiance should be also performed. The LC8 light source allows to create automatized patterns with changes on the intensity of the light with time by using the available software from a computer. As being a new equipment, this software had not been installed yet during the development of the work, and changes were done manually.
- The experiments performed and the ones proposed above should also be done with the Au and Ag samples of the first set, in case of better results are obtained with any of the samples (for example, due to the fact that the wavelength that induces the LSPR effect changes depending on the metal [44]). Also, changes on the other two metals (Pd and Pt) should also be examined, in order to find the cheapest samples with similar photocatalytic performances.
- For a deeper understand of the samples and the validation on the hypothesis stated on the present work, more resolution characterization techniques should be carried out on the samples. For example, XPS (X-ray photoelectron spectroscopy) could be used for the analysis of the oxidation states of the metals on the surface of the TiO_2 support, in order to compare differences on them before and after reaction. For the study of the morphology and structure of the metallic nanoclusters and their aggregation after the irradiation steps, HRTEM (High revolution transmission electron microscopy) could be used (e.g., to check if Pd and Pt are covered by the Ag when increasing the proportion of this last one).

7. CHAPTER 7: ECONOMIC ANALYSIS

This chapter comprises a rough estimation of the costs associated to the development of this work, including equipment, materials, chemicals and human resources needed to do it, as an approximation of the budget in case of interest in the reproduction of this work by another research group.

7.1. Cost of chemicals and materials

For the estimation of these costs, purchase costs were requested and, looking into the quantities used (number, mass or volume), the expenses were calculated, presented below.

Table 7-1. *Estimated costs of the used reagents.*

Chemical	Distributor	Purchase price	Amount used	Price
Ethanol	SCHARLAU	40 € / 5 L	0,5 L	**4,00 €**
SYLGARD™ 184 Elastomer Kit	Sigma Aaldrich	280 € / 1,1 kg	5,5 g	**1,40 €**
TiO_2 P90	EVONIK AEROXIDE	0,15 €/g	5 g	**0,75 €**
Palladium acetate	Fisher Thermo Scientific	1215 € / 10 g	0,1 g	**12,15 €**
Platinum acetylonate	Fisher Thermo Scientific	474,50 € / 5 g	0,1 g	**9,49 €**
Gold acetate	Fisher Thermo Scientific	1140 € / 5 g	0,005 g	**1,14 €**
Silver nitrate	Sigma Aaldrich	370 € / 100 g	0,05 g	**0,19 €**
Coper nitrate 3-hydrated	Sigma Aaldrich	50 € / 100 g	0,005 g	**0,003 €**
			TOTAL	**29,12 €**

From this data it can be appreciated the contribution of Pd and Pt salts to the price of the photocatalyst synthesis in front of the Ag salt, as commented in previous chapters.

Table 7-2. *Estimated costs of the employed materials.*

Material	Purchase price	Amount used	Price (€)
Dreschel bottle (Bubbler)	55 € / ud.	1	**55,00 €**
Thermocouple	40,90 € / ud.	1	**40,90 €**
Eppendorf™ Microtubes	57,65 € / 1000 uds.	25	**1,44 €**
25 ml glass powder storage bottles	23 € / 24 uds.	20	**19,17 €**
Micropipette tips	150 € / 10000 uds.	25	**0,38 €**
SS grinding bowl	500 €/ud.	1	**500,00 €**
SS grinding ball	0,5€/ball	1	**0,50 €**
Other (filter paper, parafilm, etc.)	-	-	**5,00 €** (estimated)
		TOTAL	**121,88 €**

7.2. Cost of equipment

In this case, the purchase costs were requested again, and attending on the periods of time during which each equipment was used, the cost associated was extracted from the depreciation of the equipment during that period of time, following the equation:

$$Depreciation\ cost = \frac{Purchase\ cost - Residual\ value}{Useful\ life} \qquad \textbf{(Eq. 7.1)}$$

As unknown, the residual value, the estimated value of the equipment at the end of its useful life, has been considered zero for all the equipment, while the useful lives were estimated from the manual or from reference values [52]. Results from these estimations can be seen in the following table:

Table 7-3. *Estimated costs of the employed equipment.*

Equipment	Useful life	Time used	Price (€)	Depreciation cost (€)
Oven	12 years	2 months	1700	**23,61 €**
Gas Chromatography	8-10 years	2 months	35000	**583,33 €**
Ultrasonic stirrer	8 years	2 months	300	**6,25 €**
Light source	12 years	2 months	3900	**54,17 €**
Light source lamp	1000 hours	80 hours	1800	**144,00 €**
Mass flow controller	8 years	2 months	1400	**29,17 €**
Ball mill	8 years	2 months	3400	**70,83 €**
UV Irradiance meter	8 years	2 months	300	**6,25 €**
Thermocouple data logger	15 years	2 months	507	**5,63 €**
Micropipete	8 years	2 months	100	**2,08 €**
			TOTAL	**925,33 €**

7.3. Human resources costs

For this last estimation, the salaries of the personnel involved on the project, a chemical engineering (myself) as the work developer and two doctors as director and co-director of the project, were calculated attending on the salary per hour (according to the qualification) and the time spent on the project.

Table 7-4. *Estimated costs of the personnel involved on the project*

Role	Distributor	Price (€/hour)	Nº persons	Hours worked	Price (€)
Project development	Chemical engineer	12	1	500	**6.000,00 €**
Project management	Doctor on chemical engineering	35	2	50	**3.500,00 €**
				TOTAL	**9.500,00 €**

7.4. Total costs

Finally, the total estimated budget for the development of this project is shown below:

Table 7-5. *Total estimated budget of the developed project*

Chemicals	**29,12 €**
Materials	**121,88 €**
Equipment	**925,33 €**
Human resources	**9.500,00 €**
TOTAL	**10.576,33 €**

8. CHAPTER 8: ENVIRONMENTAL IMPACT ASSESSMENT

In order to determine the short and long-term effects of the development of this project on the environment, the society and the human well-being, a brief Environmental Impact Assessment (EIA) has been performed.

Looking into the long-term effects, this project has the intention to assist in the research and development of a feasible photocatalyst for the competitive production of hydrogen with solar light, a non-polluting green technology that, with the substitution of fossil fuels by this produced hydrogen, would even promote the decarbonization of the energy supply chain. Therefore, this project could be considered to have a very positive impact on the environment in the long term.

Regarding short-term effects, referred to the work performed in the laboratory, negative impacts are also very limited. Looking into the gas emissions, from the initial gaseous stream, composed by argon, an inert gas, and water and ethanol, non-polluting gases, the mainly obtained products are hydrogen, also with no negative effect on the atmosphere, and acetaldehyde, which in turn decomposes into small quantities of other hydrocarbons (methane, propane, ethane, ethene, acetone, etc.) and CO_2. All these compounds, especially methane and CO_2, have a negative impact on the atmosphere, but the very small quantities in which they are produced (in the range of 0,01-1 μmol/min) makes this impact very limited.

The same happens with the solid wastes generated: the consumed photocatalyst contain several metals that can be potentially toxic for the environment, but the quantities in which they are used, a few milligrams, make this impact neglectable. Other important waste is plastics (gloves, pipette tips and Parafilm®), that are adequately disposed for recycling.

Finally, resource consumption can also be considered, mainly electricity by the laboratory equipment and water. The quantity of water loaded in the bubbler is very small, in the range of hundreds of millimetres once a month, while the electricity consumption is not abnormally high to be considered as an important impact.

Regarding human healthy, outside the usual laboratory safety measures, hydrogen constitutes the main risk. Hydrogen leaks are very likely to occur, and due to its high range of flammability (4%-75% in air). However, the low concentration of this compound in the gaseous stream (0.4-0.6%) and having the circuit inside the vacuum chamber reduces this possibility of accident to the minimum.

9. CHAPTER 9: REFERENCES

[1] F. Dawood, M. Anda, and G. M. Shafiullah, "Hydrogen production for energy: An overview," *International Journal of Hydrogen Energy*, vol. 45, no. 7, pp. 3847–3869, Feb. 2020, doi: 10.1016/j.ijhydene.2019.12.059.

[2] International Energy Agency, "Global CO_2 emissions rebounded to their highest level in history in 2021," Mar. 08, 2022. Accessed: May 28, 2022. [Online]. Available: https://www.iea.org/news/global-co2-emissions-rebounded-to-their-highest-level-in-history-in-2021

[3] International Energy Agency, "Data and Statistics." Accessed: May 28, 2022. [Online]. Available: https://www.iea.org/data-and-statistics/data-browser/?country=WORLD&fuel=Energy%20supply&indicator=ElecGenByFuel

[4] A. M. Oliveira, R. R. Beswick, and Y. Yan, "A green hydrogen economy for a renewable energy society," *Current Opinion in Chemical Engineering*, vol. 33, Sep. 2021, doi: 10.1016/J.COCHE.2021.100701.

[5] International Energy Agency, "World Energy Outlook 2021," 2021, Accessed: May 28, 2022. [Online]. Available: https://www.iea.org/topics/world-energy-outlook

[6] J. O. Abe, A. P. I. Popoola, E. Ajenifuja, and O. M. Popoola, "Hydrogen energy, economy and storage: Review and recommendation," *International Journal of Hydrogen Energy*, vol. 44, no. 29, pp. 15072–15086, Jun. 2019, doi: 10.1016/J.IJHYDENE.2019.04.068.

[7] National Renewable Energy Laboratory, "Hydrogen Basics." Accessed: May 28, 2022. [Online]. Available: https://www.nrel.gov/research/eds-hydrogen.html

[8] S. Z. Baykara, "Hydrogen: A brief overview on its sources, production and environmental impact," *International Journal of Hydrogen Energy*, vol. 43, no. 23, pp. 10605–10614, Jun. 2018, doi: 10.1016/J.IJHYDENE.2018.02.022.

[9] M. Hermesmann and T. E. Müller, "Green, Turquoise, Blue, or Grey? Environmentally friendly Hydrogen Production in Transforming Energy Systems," *Progress in Energy and Combustion Science*, vol. 90, p. 100996, May 2022, doi: 10.1016/j.pecs.2022.100996.

[10] L. M. Gandía, G. Arzamendi, and P. M. Diéguez, "Renewable Hydrogen Energy: An Overview," *Renewable Hydrogen Technologies: Production, Purification, Storage, Applications and Safety*, pp. 1–17, Jan. 2013, doi: 10.1016/B978-0-444-56352-1.00001-5.

[11] R. M. Navarro Yerga, M. C. Alvarez-Galván, F. Vaquero, J. Arenales, and J. L. G. Fierro, "Hydrogen Production from Water Splitting Using Photo-Semiconductor Catalysts,"

Renewable Hydrogen Technologies: Production, Purification, Storage, Applications and Safety, pp. 43–61, Jan. 2013, doi: 10.1016/B978-0-444-56352-1.00003-9.

[12] A. Rakshit and A. Suresh C., *Photocatalysis. Principles and applications*, 1st Edition. New York: CRC Press Taylor & Francis Group, 2017.

[13] B. Ohtani, "Principle of Photocatalysis and Design of Active Photocatalysts," *New and Future Developments in Catalysis: Solar Photocatalysis*, pp. 121–144, 2013, doi: 10.1016/B978-0-444-53872-7.00006-6.

[14] ChemistryDocs.Com, "Photocatalysis Types, Mechanism and Applications." Accessed: May 28, 2022. [Online]. Available: https://chemistrydocs.com/photocatalysis-types-mechanism-and-applications/

[15] K. K. Paul and P. K. Giri, "Plasmonic Metal and Semiconductor Nanoparticle Decorated TiO_2-Based Photocatalysts for Solar Light Driven Photocatalysis," *Encyclopedia of Interfacial Chemistry: Surface Science and Electrochemistry*, pp. 786–794, Jan. 2018, doi: 10.1016/B978-0-12-409547-2.13176-2.

[16] H. Eidsvåg, S. Bentouba, P. Vajeeston, S. Yohi, and D. Velauthapillai, "TiO_2 as a Photocatalyst for Water Splitting—An Experimental and Theoretical Review," *Molecules*, vol. 26, no. 6, p. 1687, Mar. 2021, doi: 10.3390/MOLECULES26061687.

[17] S. Martha, P. Chandra Sahoo, and K. M. Parida, "An overview on visible light responsive metal oxide based photocatalysts for hydrogen energy production," *RSC Advances*, vol. 5, no. 76, pp. 61535–61553, Jul. 2015, doi: 10.1039/C5RA11682A.

[18] V. Kumaravel, S. Mathew, J. Bartlett, and S. C. Pillai, "Photocatalytic hydrogen production using metal doped TiO_2: A review of recent advances," *Applied Catalysis B: Environmental*, vol. 244, pp. 1021–1064, May 2019, doi: 10.1016/J.APCATB.2018.11.080.

[19] V. Kumaravel, S. Mathew, J. Bartlett, and S. C. Pillai, "Photocatalytic hydrogen production using metal doped TiO_2: A review of recent advances," *Applied Catalysis B: Environmental*, vol. 244, pp. 1021–1064, May 2019, doi: 10.1016/J.APCATB.2018.11.080.

[20] H. Lu, J. Zhao, L. Li, L. Gong, J. Zheng, and L. Zhang, "Selective oxidation of sacrificial ethanol over TiO_2-based photocatalysts during water splitting," *Energy & Environmental Science*, vol. 4, no. 9, pp. 3384–3388, Aug. 2011, doi: 10.1039/C1EE01476E.

[21] A. v. Puga, A. Forneli, H. García, and A. Corma, "Production of H2 by Ethanol Photoreforming on Au/TiO_2," *Advanced Functional Materials*, vol. 24, no. 2, pp. 241–248, Jan. 2014, doi: 10.1002/ADFM.201301907.

[22] M. Murdoch, G. I. N. Waterhouse, M. A. Nadeem, J. B. Metson, and J. Llorca, "The effect of gold loading and particle size on photocatalytic hydrogen production from ethanol over Au/TiO_2 nanoparticles," *Nature Chemistry*, vol. 3, no. 6, pp. 489–492, May 2011, doi: 10.1038/nchem.1048.

[23] M. Schreck and M. Niederberger, "Photocatalytic Gas Phase Reactions," *Chemistry of Materials*, vol. 31, no. 3, pp. 597–618, Feb. 2019, doi: 10.1021/ACS.CHEMMATER.8B04444/ASSET/IMAGES/MEDIUM/CM-2018-04444Y_0015.GIF.

[24] A. Holm, M. Hamandi, F. Simonet, B. Jouguet, F. Dappozze, and C. Guillard, "Impact of rutile and anatase phase on the photocatalytic decomposition of lactic acid," *Applied Catalysis B: Environmental*, vol. 253, pp. 96–104, Sep. 2019, doi: 10.1016/J.APCATB.2019.04.042.

[25] J. Zhang, P. Zhou, J. Liu, and J. Yu, "New understanding of the difference of photocatalytic activity among anatase, rutile and brookite TiO_2," *Physical Chemistry Chemical Physics*, vol. 16, no. 38, pp. 20382–20386, Sep. 2014, doi: 10.1039/C4CP02201G.

[26] A. Gallo, M. Marelli, R. Psaro, V. Gombac, T. Montini, and P. Fornasiero, "Bimetallic Au–Pt/TiO_2 photocatalysts active under UV-A and simulated sunlight for H_2 production from ethanol," *Green Chemistry*, vol. 14, no. 2, pp. 330–333, Jan. 2012, doi: 10.1039/C2GC16112E.

[27] K. Sytwu, M. Vadai, and J. A. Dionne, "Bimetallic nanostructures: combining plasmonic and catalytic metals for photocatalysis," *Advances in Physics*, vol. 4, no. 1, Jan. 2019, doi: 10.1080/23746149.2019.1619480.

[28] Y. Liu, Z. Sun, and Y. H. Hu, "Bimetallic cocatalysts for photocatalytic hydrogen production from water," *Chemical Engineering Journal*, vol. 409, p. 128250, Apr. 2021, doi: 10.1016/J.CEJ.2020.128250.

[29] Y. H. Li, J. Y. Li, and Y. J. Xu, "Bimetallic nanoparticles as cocatalysts for versatile photoredox catalysis," *EnergyChem*, vol. 3, no. 1, p. 100047, Jan. 2021, doi: 10.1016/J.ENCHEM.2020.100047.

[30] Dow Chemical Company, "SYLGARD™ 184 Silicone Elastomer Technical Data Sheet," 2017. Accessed: May 29, 2022. [Online]. Available: www.consumer.dow.com

[31] Hamamatsu Photonics, "LIGHTNINGCURE Spot light source LC8 L9588." Accessed: Jun. 04, 2022. [Online]. Available: https://www.hamamatsu.com/eu/en/product/light-and-radiation-sources/lamp-module_unit/spot-light-source/L9588.html

[32] Agilent Technologies, "Agilent 490 Micro Gas Chromatograph User Manual," 2014. Accessed: May 29, 2022. [Online]. Available: https://www.agilent.com/cs/library/usermanuals/public/G3581-90001.pdf

[33] Linde, "Gas chromatography." Accessed: May 29, 2022. [Online]. Available: http://hiq.linde-gas.com/en/analytical_methods/gas_chromatography/index.html

[34] Linde, "Thermal conductivity detector (TCD)." Accessed: May 29, 2022. [Online]. Available: http://hiq.linde-gas.com/en/analytical_methods/gas_chromatography/thermal_conductivity_detector.html

[35] Y. Chen, L. Soler, C. Xie, X. Vendrell, D. Crespo, and J. Llorca, "A straightforward method to prepare supported Au clusters by mechanochemistry and its application in photocatalysis," *Applied Materials Today*, vol. 21, p. 100873, Dec. 2020, doi: 10.1016/J.APMT.2020.100873.

[36] FRITSCH, "Mini-Mill PULVERISETTE 23." Accessed: Jun. 03, 2022. [Online]. Available: https://www.fritsch.es/preparacion-de-muestras/molienda/molinos-de-bolas/details/product/pulverisette-23/

[37] Y. Chen, L. Soler, M. Armengol-Profitós, C. Xie, D. Crespo, and J. Llorca, "Enhanced photoproduction of hydrogen on Pd/TiO2 prepared by mechanochemistry," *Applied Catalysis B: Environmental*, vol. 309, p. 121275, Jul. 2022, doi: 10.1016/J.APCATB.2022.121275.

[38] EDINBURGH INSTRUMENTS, "What is Raman Spectroscopy?" Accessed: Jun. 04, 2022. [Online]. Available: https://www.edinst.com/blog/what-is-raman-spectroscopy/

[39] HORIBA Scientific, "What is Raman Spectroscopy?" Accessed: Jun. 04, 2022. [Online]. Available: https://www.horiba.com/deu/scientific/technologies/raman-imaging-and-spectroscopy/raman-spectroscopy/

[40] Surface Science Western, "Scanning Electron Microscopy coupled with Energy Dispersive X-ray (SEM/EDX) Spectroscopy." Accessed: Jun. 04, 2022. [Online]. Available: https://www.surfacesciencewestern.com/analytical-services/scanning-electron-microscopy-coupled-with-energy-dispersive-x-ray-semedx-spectroscopy/

[41] M. Abd Mutalib, M. A. Rahman, M. H. D. Othman, A. F. Ismail, and J. Jaafar, "Scanning Electron Microscopy (SEM) and Energy-Dispersive X-Ray (EDX) Spectroscopy," *Membrane Characterization*, pp. 161–179, Jan. 2017, doi: 10.1016/B978-0-444-63776-5.00009-7.

[42] Tip Biosystems, "Spectrophotometry." Accessed: Jun. 10, 2022. [Online]. Available: https://tipbiosystems.com/blog/spectrophotometry/

[43] H. Bahruji, M. Bowker, P. R. Davies, D. J. Morgan, C. A. Morton, and T. A. Egerton, "Rutile TiO_2–Pd Photocatalysts for Hydrogen Gas Production from Methanol Reforming," *Topics in Catalysis*, vol. 58, no. 2, pp. 70–76, Dec. 2014, doi: 10.1007/S11244-014-0346-9.

[44] S. Peiris, J. McMurtrie, and H. Y. Zhu, "Metal nanoparticle photocatalysts: emerging processes for green organic synthesis," *Catalysis Science & Technology*, vol. 6, no. 2, pp. 320–338, Jan. 2016, doi: 10.1039/C5CY02048D.

[45] O. Tokode, R. Prabhu, L. A. Lawton, and P. K. J. Robertson, "Controlled periodic illumination in semiconductor photocatalysis," *Journal of Photochemistry and Photobiology A: Chemistry*, vol. 319–320, pp. 96–106, Mar. 2016, doi: 10.1016/J.JPHOTOCHEM.2015.12.002.

[46] E. Korovin, D. Selishchev, A. Besov, and D. Kozlov, "UV-LED TiO_2 photocatalytic oxidation of acetone vapor: Effect of high frequency controlled periodic illumination," *Applied Catalysis B: Environmental*, vol. 163, pp. 143–149, Feb. 2015, doi: 10.1016/J.APCATB.2014.07.034.

[47] C. Dessal, L. Martínez, C. Maheu, T. Len, L. Soler, and J. Llorca, "Influence of Pt particle size and reaction phase on the photocatalytic performances of ultradispersed Pt/TiO_2 catalysts for hydrogen evolution," *Journal of Catalysis*, vol. 375, pp. 155–163, Jul. 2019.

[48] A. Gallo, M. Marelli, R. Psaro, V. Gombac, and T. Montini, "Bimetallic Au–Pt/TiO_2 photocatalysts active under UV-A and simulated sunlight for H_2 production from ethanol," *Green Chemistry*, vol. 14, no. 2, pp. 330–333, Jan. 2012, doi: 10.1039/C2GC16112E.

[49] F. D. Hardcastle, "Raman Spectroscopy of Titania (TiO_2) Nanotubular Water-Splitting Catalysts," *J Ark Acad Sci*, vol. 65, Jan. 2011, doi: 10.54119/JAAS.2011.6504.

[50] A. R. Zanatta, "A fast-reliable methodology to estimate the concentration of rutile or anatase phases of TiO_2," *AIP Advances*, vol. 7, p. 75201, 2017, doi: 10.1063/1.4992130.

[51] A. Gutés, C. Carraro, and R. Maboudian, "Silver dendrites from galvanic displacement on commercial aluminum foil as an effective SERS substrate," *J Am Chem Soc*, vol. 132, no. 5, pp. 1476–1477, Feb. 2010, doi: 10.1021/JA909806T/SUPPL_FILE/JA909806T_SI_001.PDF.

[52] University of Maryland Baltimore, "Equipment Purchases and Depreciation - Appendix F: Equipment Useful Lives." Accessed: Jun. 07, 2022. [Online]. Available: https://www.umaryland.edu/cost/about-the-office/service-center/equipment-purchases-and-depreciation/

Annex A: Photographic Report of Experimental Work

In this annex are gathered the descriptive images of the experimental work developed in the laboratory, including the synthesis and sample preparation procedures and the resultant set-up of the photocatalytic process.

A1. Synthesis Process of the Photocatalytic Powder

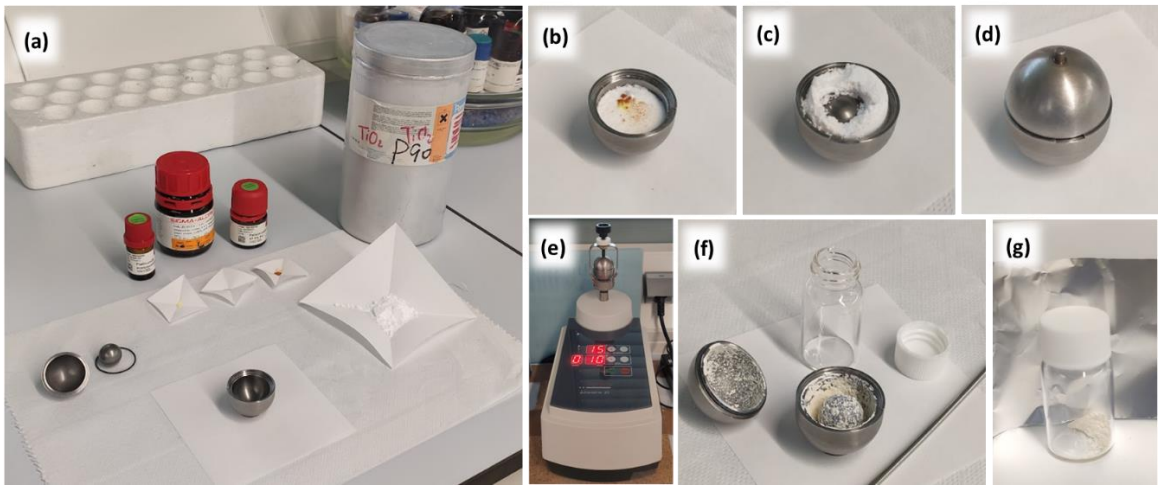

Figure A.1. *(a) Weighted required reagents to be introduced in the grinding bowl; (b) introduction of the reactants into the bowl; (c) introduction of the grinding ball; (d) closure of the bowl; (e) ball milling, with set frequency and milling time; (f) resultant powder; (g) extracted powder ready to storage.*

A2. Preparation of the Impregnated Sample

Figure A.2. *(a) Weighted powder to be impregnated; (b) filter paper, powder suspension in ethanol and micropipette; (c) resultant impregnated photocatalytic sample.*

A3. Reactor Assembly with the Sample

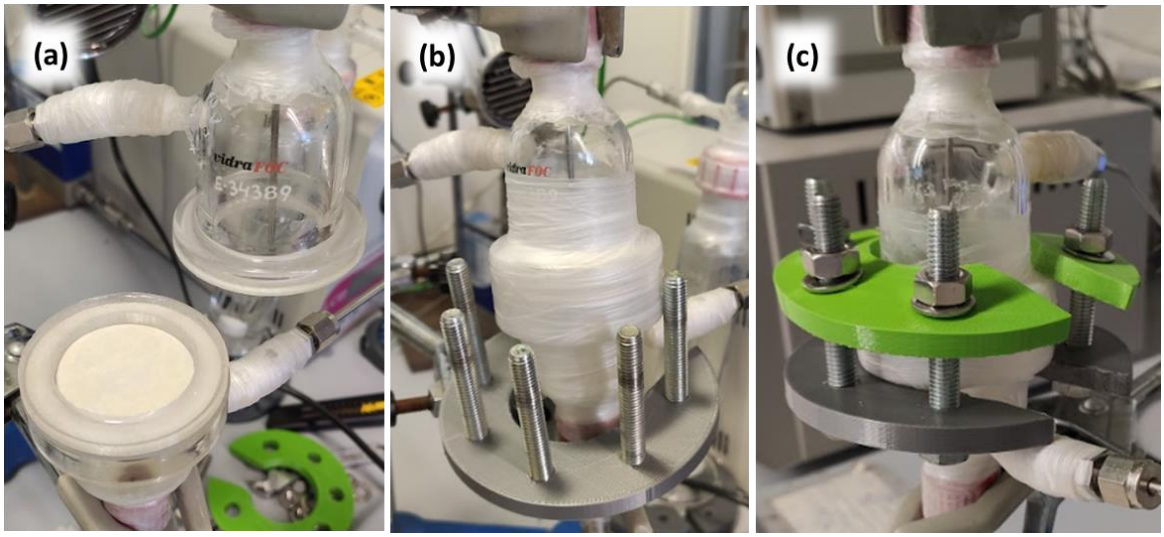

Figure A.3. *(a) Placement of the photocatalytic sample and the PDMS O-ring between the two halves of the reaction; (b) closure of the reaction and wrapping with Parafilm®; (c) sealed reactor by the pressing of the 3D printed pieces.*

A4. Resultant photocatalytic reaction system

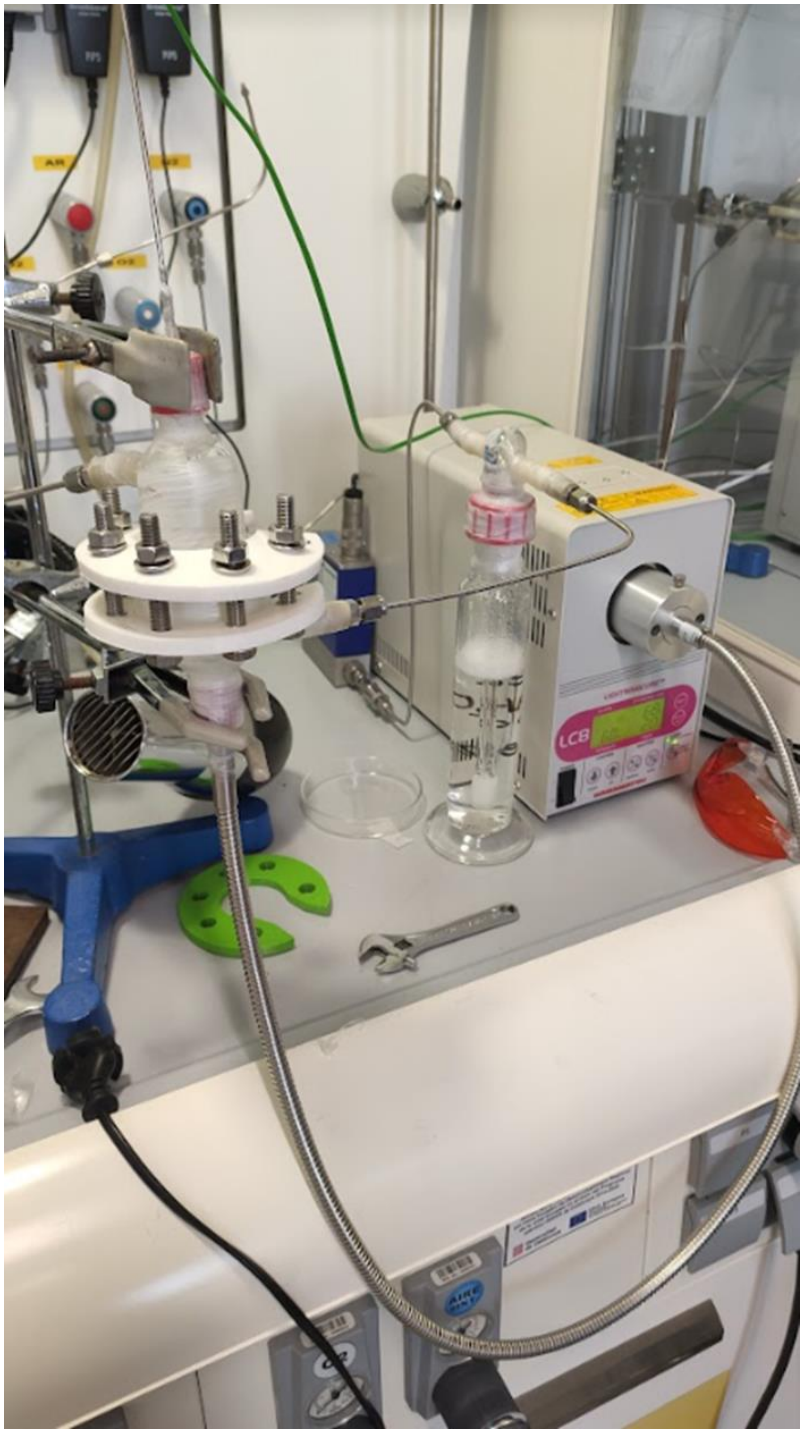

Figure A.4. *Implemented reaction system ready for operation, following the layout presented in Section 3.1.*

Annex B: Experimental Temperature Conditions

In this annex examples of the temperatures at which the experiments took place are shown, in case it is wanted to be consulted.

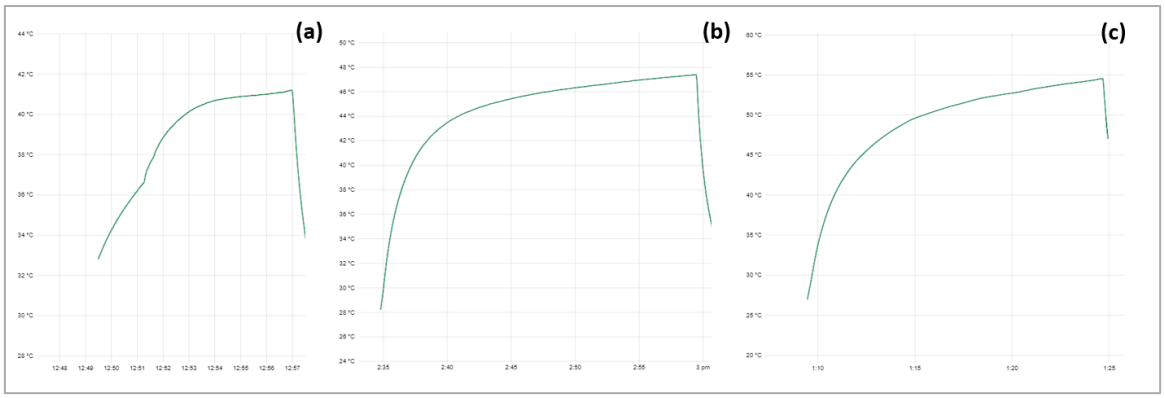

Figure B.1. *Temperature profiles comparison at different intensities of UV + Visible light (without reaction). (a) Irad = 65 mW/cm^2; (b) Irad = 85 mW/cm^2; (c) Irad = 105 mW/cm^2.*

The test showed in **Figure B.1** represents the initial attempt of choosing the irradiance for the experiments. The idea was to choose the highest irradiance at which the temperature did not surpass 55-60 ºC in order to not harm the sample (and also to avoid the unlikely event of paper burning due to the high flammability of the hydrogen), so 105 mW/cm^2 were chosen. However, due to the exothermicity of the reaction, this imposed temperature threshold was surpassed in the first set of experiments, as shown in **Figure B.2**.

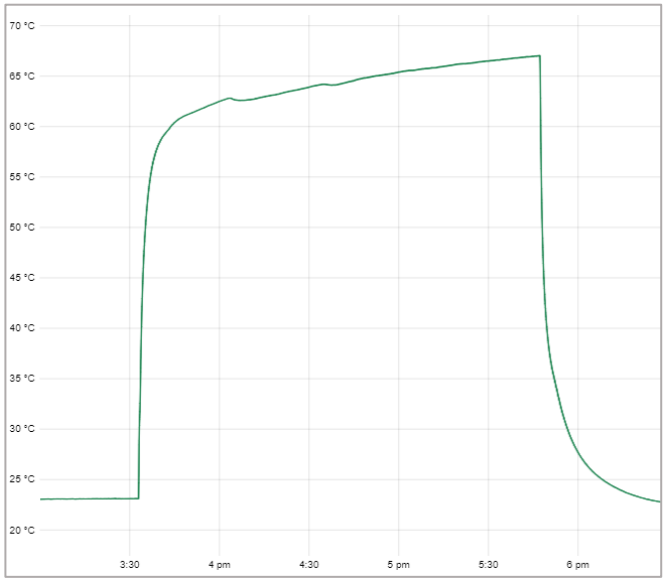

Figure B.2. *Example of temperature profile with UV + Visible light and I_{rad}=105 mW/cm^2.*

So, for the rest of the sets, 85 mW/cm^2 were chosen instead, obtaining in the experiments the temperature profiles shown below. It can be seen like temperatures are maintained in the desired range in the case of UV + Visible light, while for the UV light steps, it is raised to that range by an external heat source.

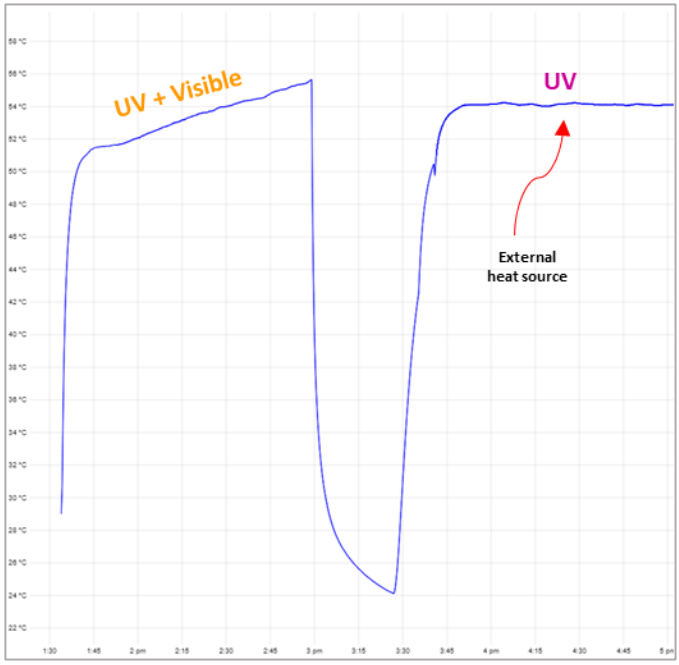

Figure B.3. *Example of temperature profile with UV + Visible and UV light steps, I_{rad}=85 mW/cm^2.*

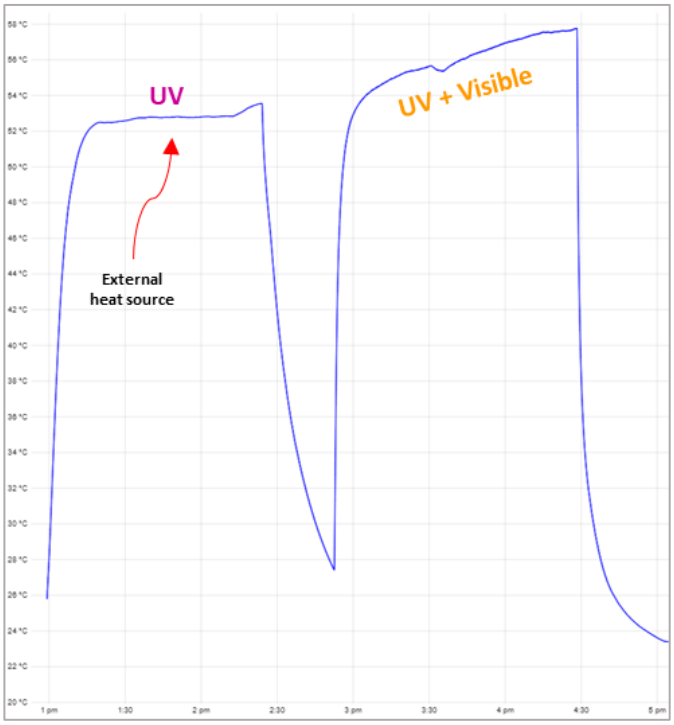

Figure B.4. *Example of temperature profile with UV and UV + Visible light steps, I_{rad}=85 mW/cm^2.*